ARCHER

Collaborative Project (CP)

Co-funded by the European Commission under the
Euratom Research and Training Programme on Nuclear
Energy within the Seventh Framework Programme

Grant Agreement Number : 269892

Start date : 01/02/2011 Duration : 48 Months
www.archer-project.eu

Advanced Reactor for Cogeneration of Heat & Electricity-R&D

generic validation of RANS and LES CFD approaches for dust behaviour using existing reference DNS DB

Authors : JAYARAJU Santhosh (NRG) , Pratap Sathiah, Henny Bijleveld, Ferry Roelofs (all NRG)

ARCHER - Contract Number: 269892
Advanced High-Temperature Reactors for Cogeneration of Heat and Electricity R&D
EC Scientific Officer: Dr. Panagiotis Manolatos

Document title	generic validation of RANS and LES CFD approaches for dust behaviour using existing reference DNS DB
Author(s)	JAYARAJU Santhosh , Pratap Sathiah, Henny Bijleveld, Ferry Roelofs (all NRG)
Number of pages	65
Document type	Deliverable
Work Package	WP 23
Document number	D23.51
Issued by	NRG
Date of completion	21/03/2014
Dissemination level	Confidential, only for members of the consortium (including the Commission Services).

Summary

This document contains the generic validation for the RANS and LES CFD approaches to predict the particle transport and deposition. Detailed literature review is performed to collect and evaluate the available experimental and DNS data pertaining to the particle deposition validation. In case of RANS modelling, several uncertainties regarding the near-wall modelling are addressed. A robust and well validated RANS model coupled with a specific near-wall correlation is proposed for the accurate particle transport and deposition predictions. On the other hand, the capability of a more advanced model such as the LES is validated by performing two test cases.

Approval

Date	By
21/03/2014	Karl VERFONDERN
21/03/2014	Norbert KOHTZ
21/03/2014	Steven KNOL

Distribution list

Name	Organisation	Comments
P. Manolatos	EC DG RTD	Through the EC participant portal
All beneficiaries	ARCHER	Through the private online workspace

Generic validation of RANS and LES CFD approaches against existing DNS database

Santhosh Jayaraju, Pratap Sathiah and Henny Bijleveld

NRG-2.2902/14.125436/S&P/STJ/NP
March 21, 2014

ARCHER Deliverable 23.51

author :	Santhosh Jayaraju	reviewed :	Henny Bijleveld
	Santhosh		Henny Bijleveld
63 pages		approved :	Ferry Roelofs

Contents

1 Summary

This document contains the generic validation for the RANS and LES CFD approaches to predict the particle transport and deposition. Detailed literature review is performed to collect and evaluate the available experimental and DNS data pertaining to the particle deposition validation. In case of RANS modelling, several uncertainties regarding the near-wall modeling are addressed. A robust and well validated RANS model coupled with a specific near-wall correlation is proposed for the accurate particle transport and deposition predictions. On the other hand, the capability of a more advanced model such as the LES is validated by performing two test cases.

2 Introduction

A very high temperature (VHTR) or high temperature gas cooled reactor (HTGR) is under consideration as a fourth generation advanced nuclear reactor. The reactor uses graphite as a moderator and helium gas as a coolant. Because of high core outlet temperature, high thermal efficiency is achieved in these types of reactors. Moreover, there is no need for active safety systems to cool the reactor core as it is designed to lose heat by itself from natural circulation. A number of experimental and prototype reactors have been built and operated in the past. Examples of high temperature reactors are the Dragon reactor (United Kingdom), the Peach Bottom reactor (United States of America), AVR and THTR 300 (Germany) and the reactor at Fort St. Vrain (United States of America). At present, there are experimental reactors under operation in Japan (HTTR) and China (HTR-10). Apart from this, two full scaled HTGRs, the two-module plat HTR-PM, are under construction in China.

The core design in these types of reactors is generally based on prismatic or pebble bed arrangement. In a typical pebble bed reactor, the reactor core consists of randomly stacked pebbles. Typically there are several hundred thousands of them in the core. These pebbles are primarily made of graphite and contain uranium dispersed in sand-size grains throughout the pebble. One of the main sources of dust production is due to the abrasion of randomly stacked graphite pebbles. The generated dust is essentially composed of carbonaceous compounds, fission and activation products. In a 400 MW thermal pebble-bed HTR, abraded dust is anticipated to be in the range of 30-100 kg/yr [1]. The dust is eventually carried by helium gas through the primary circuit and gets deposited in its main components such as the main pipes systems, the heat exchangers (steam, generators, intermediate heat exchangers or recuperators) and turbo-machinery if applicable. Remobilisation of dust deposited in the primary system is identified as one of the foremost concerns during a potential accident [2]. Hence, accurate prediction of dust transport and deposition is an important step in the design of this type of reactors.

2.1 Dust size distribution in (V)HTR

The main knowledge base comes from a small number of test reactors which were mostly built, operated and decommissioned between 1960s and 1990s [2]. While studying the nature of the dust from these sources, Kissane et al. [2] and [1] suggest that the information might well be misleading with respect to the modern designs and should be interpreted wisely. The authors have reported many sources related to the dust size distribution:

- Dust size measured at the end of life cycle of the pebble-bed AVR was found to be largely sub-micron with a geometric mean diameter of 0.6μm [3].

- The above information can be influenced by the oil ingress incident in 1982. Measurements in early life of AVR indicated an average dust particle size of 5μm [2].
- Recent experiments for HTR-10 generating dust by pebble abrasion indicate a geometric-mean diameter of about 2.2μm [4]. In terms of number of particles, 90% of them were $\leq$6μm in diameter.
- Kissane et al. [2] and [1] finally conclude that the dust generated in a V(HTR) will be approximately $<$10μm.

Referring to the dust particles found in the AVR test reactor, Komen [5] reports that the particle range was between 0.4μm and 4μm, with most of the dust located between 0.5μm and 1.5μm.

For the present study, particles in range of *0.1μm to 10μm* are considered to cover all the ranges of particle sizes observed in the literature.

2.2 Flow characteristics in (V)HTR

The dust accumulation within the primary system of an HTR can be broadly divided in regions such as main piping systems and heat conversion components. The following considerations are based on the regions identified by Komen [5] in the direct cycle PBMR 400, i.e. the main pipe systems, the turbo-machinery, and the recuperators. The characteristic geometry and flow parameters in these three regions are summarized in Table. 1

Helium is taken to be the working fluid. For conditions of 5MPa and 700K, the following gas properties are considered:

- The gas density ρ_g=3.4 kg/m^3.
- The dynamic viscosity μ_g=3.6 $\cdot 10^{-5}$ $Pa.s$

Based on Baumer et al. [6], the volume fraction of the dust is estimated to be between 2.9 $\cdot 10^{-12}$-12 to 2.9$\cdot 10^{-10}$. The corresponding dust number density is estimated to be between 5.5$\cdot 10^{6}$ to 5.5$\cdot 10^{8}$ $particles/m^3$.

Based on the region of interest in the flow domain, we can define two flow time-scales.

- Time scale of large turbulent eddies (τ_L)
- Average time scale of near-wall eddies ($\tau_{near-wall}$)

Table 1 Tentative estimates of the characteristic geometry and flow parameters.

	Geometric Length Scale L (m)	Main Velocity Scale U (m/s)	Flow Reynolds number UL/v	Time scale of large eddies τ_L=0.1L/0.1U (s)	Time scale of average near-wall eddies $\tau_{near\text{-}wall}=(\nu/u_\tau^2)$ (s)
Main pipe system	0.7	65	4.3e6	1.08e-2	3.85e-6
Turbo-machinery	0.1	175	1.65e6	5.71e-4	4.19e-7
Recuperators	0.00066	10	623	6.6e-5	1.79e-5

The time scale of large turbulent eddies (τ_L) can be estimated as

$$\tau_L = \frac{0.1 * L}{0.1 * U} \quad [s] \tag{1}$$

$0.1 * L_L$ is the length scale of the large eddy which is taken to be 10% of the characteristic geometry length. $0.1 * U$ is the velocity scale of the large eddy which is taken to be 10% of the mean velocity.

The average time-scale of the near-wall eddies ($\tau_{near-wall}$) can be estimated as [5]:

$$\tau_{near-wall} = \frac{\nu}{{u_\tau}^2} \quad [s] \tag{2}$$

ν is the kinematic viscosity of the fluid. The friction velocity u_τ can be estimated based on the skin friction coefficient which is [7]:

$$C_f = \frac{\tau_w}{(1/2)\rho U^2} = \frac{{u_\tau}^2}{(1/2)U^2} \tag{3}$$

Based on 1/7 power law with experimental calibration given by Schlichting [8], C_f is given by:

$$C_f = \frac{0.0592}{Re^{0.25}} \tag{4}$$

Even though the formulation is derived for a flat plate, it can be used as a first approximation for a turbulent boundary layer.

2.3 Particle response time

The particle momentum response time is defined as the time required for a particle released from rest, to achieve 63% of the velocity of the carrier fluid. For spherical particles at low particle Reynolds numbers (< 0.3), the response time can be estimated as:

$$\tau_p = \frac{\rho_p {d_p}^2}{18\mu_g} \quad [s] \tag{5}$$

For a particle density ρ_p of 1250 kg/m^3, the following particle response times are obtained for different particle diameters:

$$\tau_p(0.1\mu m) = 2 \cdot 10^{-8} \quad [s] \tag{6}$$
$$\tau_p(1\mu m) = 2 \cdot 10^{-6} \quad [s] \tag{7}$$
$$\tau_p(5\mu m) = \cdot 510^{-5} \quad [s] \tag{8}$$
$$\tau_p(10\mu m) = 2 \cdot 10^{-4} \quad [s] \tag{9}$$

2.4 Stokes number

The Stokes number defines the relationship between the particle response time and the fluid time scale. It is defined as:

$$Stk = \frac{\text{Particle response time}}{\text{fluid time scale}} \tag{10}$$

As defined before, the fluid time scale can be defined in two different scales based on the region of interest. If we are interested in the bulk flow, then the fluid time scale will be τ_L. If we are interested in the average near wall region, then $\tau_{near-wall}$ becomes important.

For the sake of interpretation, lets consider the bulk as the region of interest. If the particle response time τ_p is much smaller than the time scale of the large eddies in the flow τ_L, then the particles will have enough time to respond to the changes in the large(mean) flow structures. $\tau_p \ll \tau_L$ ($Stk_{large-eddy} \ll 1$) implies that the particles will easily adapt to the changes in the mean flow and will have local velocities similar to that of the fluid. On the other hand, if $\tau_p > \tau_L$ ($Stk_{large-eddy} > 1$) , particles will not feel all the changes happening in the mean flow structures.

If we consider a 90 degree bent pipe flow, the particles which satisfy $Stk_{large-eddy} \ll 1$ will follow the changes in the flow direction and reach the outlet. On the other hand, the particles with $Stk_{large-eddy} > 1$ will not be able to follow the flow curvature at the 90 degree bend region and hence tend to impact on the wall due to higher particle inertia.

Table 2 Tentative estimates of the Stokes numbers.

	Time scale (response time) of particles $\tau_p = \rho_p d_p^2/18\mu_f$ (s)	$Stk_{large-eddy}$ τ_p/τ_L	$Stk_{near-wall}$ $\tau_p/\tau_{near-wall}$
Main pipe system	1.93e-8(d_p=0.1μm) 1.93e-6(d_p=1μm) 4.82e-5(d_p=5μm) 1.93e-4(d_p=10μm)	1.79e-6 1.79e-4 4.48e-3 1.79e-2	5e-3 0.5 12.5 50
Turbo-machinery		3.38e-5 3.38e-3 0.0844 0.338	0.0461 4.61 115 461
Recuperators		2.92e-4 0.029 0.731 2.92	1.08e-3 0.108 2.7 10.8

Table 2 summarizes all typical Stokes number estimates for the present application. As seen, $Stk_{large-eddy}$ is less than 1 for most of the particle diameters in all three regions. This means, most particles will have enough time to respond to the changes in the large flow structures. On the other hand, $Stk_{near-wall}$ shows a wide range of Stokes number ranging form very small to big, meaning that the behavior of the particle depends on the particle size under consideration.

2.5 Deposition mechanisms

Deposition mechanisms can be best understood by taking an example of deposition in a smooth pipe flow. Fig. 1 shows the typical characteristic regimes of dimensionless deposition velocity as a function of dimensionless particle relaxation time which is adapted from [9]. Please note that the dimensionless particle relaxation time is nothing but $Stk_{near-wall}$. Since the particle deposition is directly related to the interaction of particles with the near-wall eddies, $Stk_{near-wall}$ is generally used in literature to characterize the different deposition regimes.

As shown in the figure, the most common classification of deposition in a smooth pipe is divided into three regimes, namely *the diffusional deposition regime, the diffusion-impaction regime, and the inertia-impaction regime.*

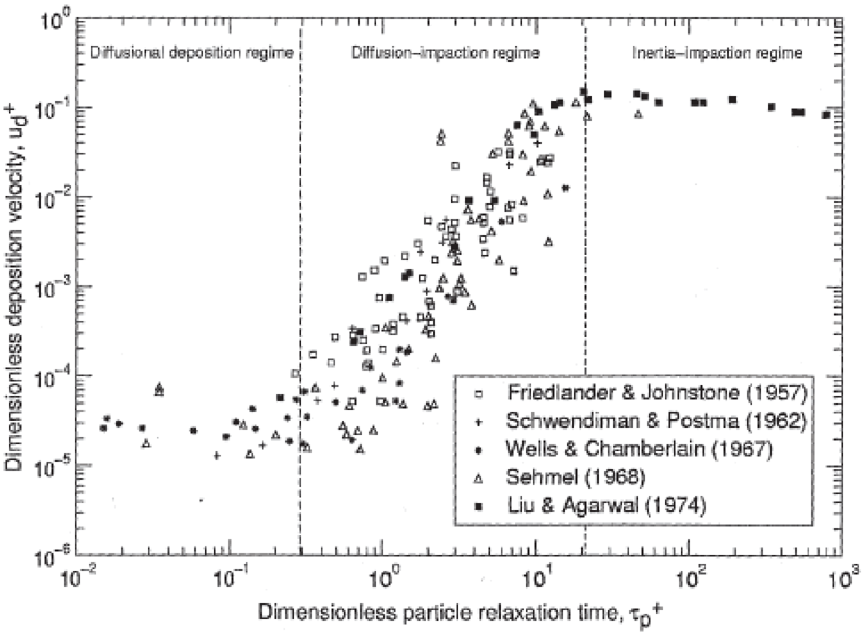

Figure 1 Characteristic regimes of dimensionless deposition velocity as a function of dimensionless particle relaxation time [9].

If τ^+ $(Stk_{near-wall})$ is smaller than about 0.25, the particles are small enough to respond to the changes in the near-wall turbulent flow motions. As a result, Brownian motion becomes an important mechanism for the particle deposition. This regime is indicated as *the diffusional deposition regime.*

If τ^+ is bigger than about 20, then the particles have practically no time to respond to the changes in the near-wall flow motions. Instead, their motion might only be affected by the larger eddies in the bulk of the flow. Consequently, these large particles deposit on the walls through momentum given to them by the large eddies. This regime is indicated as *the inertia-impaction regime or the inertia-moderated regime.*

If τ^+ is in the approximate range between 0.25 and 20, the particles are expected to only partly follow the near-wall eddies. Such particles either shoot ahead or lag behind the near-wall eddies. Hence, these particles may get deposited either due to Brownian motion or by impaction. This regime is indicated a *the diffusion-impaction regime or the turbulent eddy impaction regime.*

Komen [5] has performed extensive literature review on different models which are used in the literature for particle transport and deposition in the main coolant pipes, turbo-machinery and the recuperators. Using these models, Komen [5] has performed first hand calculations to estimate the probable deposition mechanisms based on relevant flow and dust parameters. The same is summarized in Fig. 2.

	Deposition mechanism
Main pipe system	- **Turbulent eddy impaction** – most important - **Gravity** – important (atleast 1 ord of magnitude less than turb eddy impaction) - Brownian diffusion – can be neglected
Turbo-machinery	- **Turbulent eddy impaction** – most important for d_p <~1.5 µm - **Inertial Impaction** – most important for d_p >~1.5 µm - Gravity and Brownian diffusion – can be neglected
Recuperators	- **Thermophoresis** – most important - **Gravity** – Important - Brownian diffusion – can be neglected

Figure 2 Estimated deposition mechanisms in the main coolant pipes, turbo-machinery and the recuperators based on Komen [5].

3 Validation database

There are several Direct-Numerical-Simulation (DNS) and experimental data of particle transport and deposition available in the literature which can be used for code development and validation purpose. The DNS and the experimental database are discussed in the next sections.

3.1 DNS database

The study of particle transport and deposition in wall-bounded flows has received considerable attention due to its practical relevance to numerous industrial applications. Several experimental and numerical efforts have been made to better understand the complex phenomena of fluid-particle interaction. Even though experimental data prove to be very useful in the interpretation and understanding of the physical phenomena, generating data which are of benchmarking quality is often tedious and expensive. On the other hand, DNS for simple test-cases like channel and pipe flows has proven to be an effective tool to generate benchmark quality data which can be used towards further model development. Despite the large number of published works, it is extremely difficult to gather a uniform and complete source of data that can be used to perform a phenomenological study [10]. The reason for this is attributed to lack of uniformity and of completeness in available numerical data. In the present work, few very relevant and recent DNS simulations which can be used for the validation/model-development of particle transport and deposition are described.

Zhang & Ahmadi [11] studied the aerosol transport and deposition in vertical and horizontal turbulent channel flows in presence of different gravity directions. Navier Stokes equations are solved using DNS in a pseudo-spectral solver. The Reynolds number based on the friction velocity was Re_τ=125. The studied particle diameters were in the range between 0.01μm to 50μm. This corresponds to a non-dimensional particle relaxation time between about 0.01 to 100. The particle forces included were the Stokes drag, Brownian diffusion, lift and gravitational acceleration. The particle deposition rate as a function of time is available for various particle sizes. The deposition velocities under various conditions are also available for validation purpose.

Narayanan et al. [12] has studied the particle dispersion and deposition in the near-wall region of a turbulent channel flow. The Reynolds number based on the friction velocity was Re_τ=85.5. The range of particles studied had non-dimensional relaxation times between 5 and 15. The Stokes drag and basset forces are taken into account while the effect of gravity is neglected. The particle deposition rate as a function of time is available for various particle relaxation times. The mean and RMS velocities for both fluid and particle phase are available for comparison.

Marchioli et al. [13] performed DNS and lagrangian tracking to study the turbulent transfer and deposition of intertial particles in a vertical upward circular pipe flow. The Reynolds number based on the friction velocity was Re_τ=337. The range of particles studied had non-dimensional relaxation times between 3.2 and 111.6. The Stokes drag, buoyancy and Saffman lift forces are taken into account. The particle deposition rate with respect to time is available. The particle number density distribution along the radial direction is also provided at a given time instance.

You et al. [14] studied the motion of micro-particles in a channel flow. The mean flow Reynolds number was Re_m=3300. The particles studied had the Stokes number in range 0.001 to 11. Stokes drag was the only considered force acting on the particle. The particle number density profiles for different particle sizes are available for comparison. In addition to DNS, the authors also tested the performance of a two-equation $k - \varepsilon$ turbulence model, especially for a low Stokes number particle.

Vreman [15] performed DNS of a vertical pipe flow with Lagrangian approach for the particles. The Reynolds number based on the friction velocity was Re_τ=140. Two particles with Stokes numbers of 20 and 46 are studied. The effect of different particle mass loadings (0.11 to 30) and its influence on the interaction between the two phases is also studied. The Stokes drag force and the force due to particle-particle collision and the influence of gravity are taken into account. Mean and RMS velocities for both fluid and particle phase are available for validation purpose.

Noting the lack of uniformity and completeness in the literature, Marchioli et al. [10] set up an international collaborative benchmark test case for DNS and Lagrangian particle tracking database for turbulent particle dispersion in channel flow at low Reynolds number. The Reynolds number based on the friction velocity was Re_τ=150. The particles studied had the Stokes number in range 1 to 25. In order to minimize the number of degrees of freedom by keeping the simulation settings as simplified as possible, only the Stokes drag force is considered. The particle concentration profiles and deposition rates are available for validation purpose. The results available are reliable and accurate for model testing/development as they come from five independent simulations performed through a collaborative benchmark.

Marchioli et al. [16] further performed DNS simulations for Re_τ 150 and 300. The particles studied had the Stokes number in range 0.2 to 125. Stokes drag is the only considered particle force. Mean and RMS velocities for both fluid and particle phase are available for validation purpose. The particle number concentrations along the channel height are also provided. In the same paper, Large Eddy Simulations are also performed to assess the effect of filtering and SGS modeling of fluid phase on the particle velocity and concentration statistics.

Recently, Zamansky et al. [17] have performed DNS of a channel flow at a relatively high Reynolds number of Re_τ 587. The particles studied had the Stokes number in range 1 to 125. Mean and RMS particle velocities along the channel are available for comparison.

The above discussed literature is summarized in Table 3.

3.2 Experimental database

Apart from the DNS data, there are several useful experimental data available in literature for simple flow configurations. The most widely used experimental data are discussed below.

One of the most widely used experimental data is of Liu and Agarwal [18] who measured the deposition rate of aerosol particles in a turbulent vertical pipe flow. The mean flow Reynolds numbers were 10,000 and 50,000. The particle diameters were in the range of 1.4 to 21μm. The corresponding particle relaxation times were in the range 0.21 to 774.

McCoy and Hanratty [19] compiled the various available experimental data of deposition rates in a vertical pipe. The particle diameters were ranging from sub-micron to several hundred microns. Based on the compiled data, McCoy and Hanratty proposed a piecewise best-fitting correlation. This correlation can be used to predict/improve the CFD model predictions.

Pui et al. [20] performed experimental study of particle deposition in bends of circular cross-section. The flow Reynolds numbers studied were 100, 1000, 6000, and 10,000. The particle considered had the Stokes numbers in the range 0.03 to 1.46.

McFarland et al. [21] studied aerosol deposition in 90 degree bends for the mean flow Reynolds numbers in approximate range of 3000 to 20,000. The particles considered have Stokes number in range 0.1 to 0.7. The main objective of this work was to study the effect of curvature ratio on the aerosol penetration.

Peters et al. [22] studied particle deposition in industrial duct bends with varying angles of 45, 90 and 180 degree. The mean flow Reynolds numbers considered were 100, 1000, 6000 and 10,000. The particle Stokes numbers covered were in the range 0.08 to 16. Particular attention was given to the case with tube bend of 90 degrees.

Sippola et al. [23] also studied aerosol deposition in 90 degree bends. The particle diameters were in the range 1-16μm and the air speeds in the range 2.2-9m/s. In terms of particle Stokes number, the range was between $4.2{\cdot}10^{-3}$ to 4.2.

Recently, Jiang et al. [24] has also looked into the aerosol penetration and deposition in 90 degree bends. The particle Stokes numbers considered were in the range of $1{\cdot}10^{-4}$ to 1.

Table 3 Summary table of the recent and relevant DNS data in the literature.

Author	Type of domain	Flow & particle characteristics	Available data
Zhang et al. 2000	Vertical and horizontal duct flow	Re_τ=125 D_p=0.01 to 50µm (τ_p^+=0.01 to 100) Drag, Brownian diffusion, lift and gravity force considered.	- Wall deposition rate vs. time - Depsition velocity vs. Particle relaxation time (τ_p)
Narayanan et al. 2003	Open channel flow	Re_τ=85.5 τ_p^+=5 to 15 Drag, basset force considered.	- Wall deposition rate vs. time - Mean and RMS velocities for both fluid and particle phase.
Marchioli et al. 2003	Vertical upward circular pipe-flow	Re_τ=337 τ_p^+=3.2 to 111.6 Drag, buoyancy and Saffman lift force are considered.	- Deposition rate vs. time - Particle number density distribution in radial direction at a given time instance.
You et al. 2004	Open channel flow	Re_m=3300 Stk=0.001 to 11 Drag force is the only force considered.	- Particle number density distribution wrt to the channel height.
Vreman 2007	Vertical pipe flow	Re_τ=140 Stk=20 to 46 Mass loading: 0.11 to 30 Drag, particle-particle collision, gravity.	- Mean and RMS velocities for both fluid and particle phase.
Marchioli et al. 2008	Channel flow	Re_τ=150 Stk=1, 5 and 25 Drag force is the only force considered.	- Mean & RMS velocities for both fluid and the particle phase - Wall deposition rate vs. time.
Marchioli et al. 2008b	Channel flow	Re_τ=150 & 300 Stk=0.2 to 125 Drag force is the only force considered.	- Mean & RMS velocities for both fluid and the particle phase - Particle number density distribution wrt to the channel height.
Zamansky et al. 2011	Channel flow	Re_τ=587 Stk=1 to 125 Drag force is the only force considered.	- Mean & RMS velocities for the particle phase

4 Numerical modeling

The numerical modeling of particle transport and deposition onto the walls of turbulent flows are generally handled by the Eulerian approach or the Lagrangian approach.

In the Eulerian approach, the particles are treated as a second fluid which behaves like a continuum and the equations are developed for the average properties of the particles. For example, the particle velocity is the average velocity over a control volume. This approach is most suitable when one requires a macroscopic field description of the dispersed phase properties such as pressure, mass flux, concentration, velocity and temperature. The Eulerian approach is more suitable for simulating large-scale particle flow processes. However, this approach requires sophisticated modeling of the closure terms that result from the averaging process. These terms describe the key effects and phenomena found in industrial processes [25].

A Lagrangian approach is useful when the particle phase is so dilute that the description of particle behavior by continuum models is not feasible. The motion of a particle is expressed by ordinary differential equations in Lagrangian coordinates and are directly integrated to obtain individual tracks of particles. Since the dust in V(HTR) is expected to be dilute, we follow the lagrangian approach.

4.1 Governing equations

Based on the physical properties of dust measured in AVR, their estimated behavior in different regions of an HTR, and on the mathematical modeling effort required, there are certain reasonable assumptions made to describe the dust aerosol transport and deposition in a HTR. The major assumptions for the present work are as follows.

The dust particle is taken to be spherical: The HTR dust sizes reported in the literature are generally in terms of geometric-mean-diameter. As a first approximation, the dust particles are taken to be spherical.

The ratio of particle to fluid density is very large: The density of dust particles are generally much higher when compared to the fluid medium which is helium. Typically, the density of dust particles is of the order of $\sim 10^3\ kg/m^3$ as opposed to $\sim 3kg/m^3$ for the helium fluid.

The aerosol phase is dilute: A quantitative way of assessing a dilute versus dense flow is by taking the ratio of particle relaxation time (t_r) to the particle collision time (t_c). The particle relaxation time is defined as the time required by the particle to loose 63% of its initial velocity. If $t_c > t_r$, the particle has enough

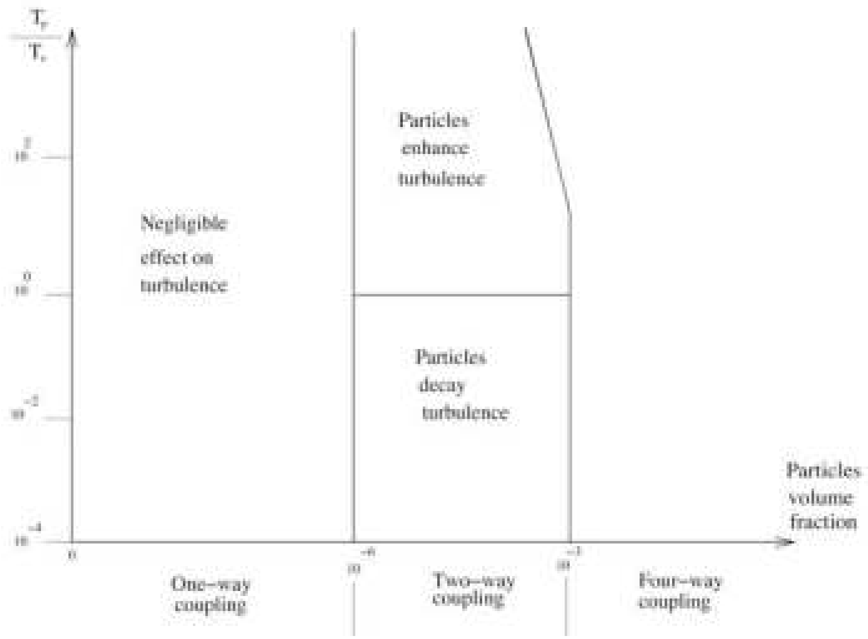

Figure 3 Map for particle-turbulence modulation [26].

time to respond to the local fluid dynamic forces before collision occurs. Hence, a dilute flow is one in which the particle motion is controlled by fluid forces such as the drag force. The estimation of collision time requires the information of relative velocity of a particle with respect to the other. It is generally hard to estimate this relative velocity. In the present work, as a first approximation, the flow is taken to be dilute.

One-way coupling: The phenomenon of mutual mass, momentum and energy transfer between the phases is termed as coupling. Elghobashi [26] proposed a map of regimes of interactions between particles and fluid turbulence which is given by Fig.3.

For values of the dispersed-phase volume fraction less than 10^{-6}, particles have negligible effects on the flow turbulence. This situation is termed as the one-way coupling. In the second regime, with dispersed-phase volume fractions between $10^{-6} - 10^{-3}$, the existence of the particles can augment the turbulence if the ratio of the particle response time to the turnover time of a large eddy is greater than unity, or can attenuate turbulence if the ratio is less than unity. This interaction is called two-way coupling. In the third regime where the volume fractions are greater than 10^{-3}, in addition to two-way coupling between particles and the flow turbulence, inter-particle collisions take place. Hence this regime is termed as four-way coupling.

Based on the estimates in HTR by Komen [5], the largest volume fraction is of the order 2.9×10^{-10}. Hence, only one-way coupling is considered in the present work.

Taking the above assumptions into consideration, the Lagrangian equations [27] governing the particle motion can be written as:

$$\frac{d\vec{x}_p}{dt} = \vec{u}_p \tag{11}$$

and

$$\frac{d\vec{u}_p}{dt} = F \tag{12}$$

where, $\vec{x_p}$ is the particle position, and $\vec{u}_p$ is the velocity of the particle. F represents all the body forces and the surface forces acting on the particle. Example of body force acting on the mass of the particle is gravity, while the surface forces are due to drag, which represents a momentum coupling between the two phases [28]. The forces, which are relevant for the present work, are the the drag, gravity and Brownian diffusion which are described below:

$$F = F_{drag} + F_{gravity} + F_{lift} + F_{brownian} \tag{13}$$

4.1.1 Drag force

Generally, the particle moves with a different velocity than the fluid at any given point. The difference in fluid velocity ($\vec{u}$) and the particle velocity ($\vec{u}_p$), is termed as the *slip velocity* ($\vec{u} - \vec{u}_p$), which leads to an unbalanced pressure distribution as well as viscous stresses on the particle surface. This yields a resulting force called a *drag force*. For a rigid sphere, the drag force for unit particle mass is given by $F_d(\vec{u} - \vec{u}_p)$. F_d is defined as [29]:

$$F_d = \frac{1}{\tau_p}\frac{C_d Re_p}{24}. \tag{14}$$

Here, the drag coefficient C_d is a function of particle Reynolds number, Re_p. Various experimental based empirical correlations for the drag coefficient as a function of Re_p are available in the literature [29]. The Reynolds number Re_p of the particle is defined as:

$$Re_p = \rho\, d_p\, \frac{|\vec{u} - \vec{u}_p|}{\mu}. \tag{15}$$

τ_p in Eq. 14 is the particle relaxation time which is defined as:

$$\tau_p = \frac{C_c \rho_p d_p^2}{18\mu} \qquad \text{for} \qquad Re_p \leq 1 \tag{16}$$

$$\tau_p = \frac{4}{3}\frac{\rho_p}{\rho}\frac{C_c d_p^2}{C_d|\vec{u} - \vec{u}_p|} \qquad \text{for} \qquad Re_p > 1 \tag{17}$$

where, d_p is the particle diameter, ρ_p is the particle density and C_c is the Cunnigham slip correction factor given by:

$$C_c = 1 + \frac{2\lambda}{d_p}\left(1.257 + 0.4e^{(1.1 d_p/2\lambda)}\right) \tag{18}$$

where, λ is the gas molecular mean free path.

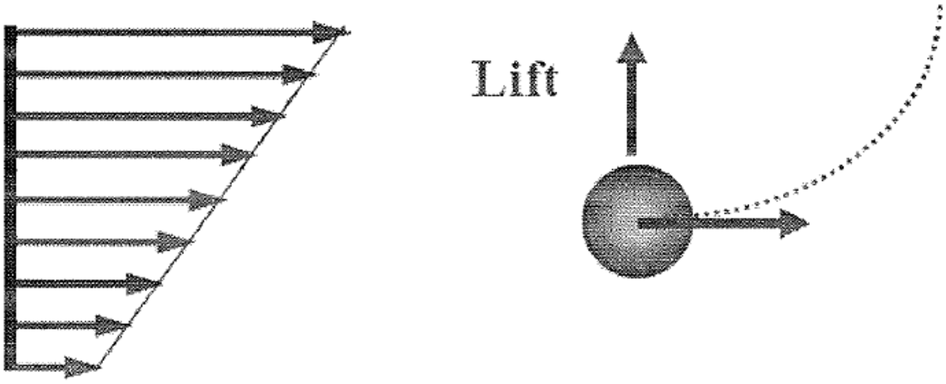

Figure 4   Particle in a constant shear flow.

4.1.2 Gravity force

A particle when subjected to a gravitational field experiences a force in the direction of the gravitational acceleration. The particle also experiences a buoyancy force opposite to the direction of gravity. This force is equal to the weight of the displaced fluid according to Archimedes principle. The net force due to gravity is given by:

$$F_{gravity} = g_x \frac{(\rho_p - \rho)}{\rho_p} \tag{19}$$

where, g_x is the gravitational acceleration in x direction, ρ and ρ_p are the density of the fluid and the particle, respectively.

4.1.3 Lift force

A particle entrained in a shear flow field may experience a shear induced lift force perpendicular to the main flow direction. For a positive fluid velocity gradient du_f/dy as shown in Fig.4, the lift force is in the positive y-direction, given that the fluid velocity u_f in streamwise direction is greater than the particle velocity u_p in the streamwise direction. Lift force becomes important close to the walls as the fluid velocity gradients as well as the difference between particle and fluid velocity are the largest here.

The lift force is given by Saffman [30], [31] as follows:

$$F_{saffman} = 1.61 {d_p}^2 (u_{f_x} - u_{p_x})(\rho_f \mu_f)^{0.5} \frac{du_f/dy}{|du_f/dy|^{0.5}} [N] \tag{20}$$

Within FLUENT, the Saffman lift force is modeled as:

$$F_{saffman} = \frac{5.188 \nu^{0.5} \rho_f d_{ij}}{\rho_p d_p (d_{lk} d_{kl})^{0.25}} (u_f - u_p) \tag{21}$$

This formulation is mainly intended for small particle Reynolds numbers and typically sub-micron particles.

4.1.4 Brownian diffusion

Any given fluid at the molecular level is associated with random molecular movements and collisions. When the particle response time becomes less than the time required for the molecular impacts in a fluid, the particles have enough time to respond to these molecular changes in the fluid. Brownian diffusion is characterized by random motion of particles where the particles generally tend to move from higher particle concentration region towards the lower particle concentration region.

Within [29], the Brownian force per unit mass is modeled as:

$$F_{brownian} = \xi_i \sqrt{\frac{\pi S_0}{\Delta t}} [N/kg] \tag{22}$$

where, S_0 is the spectral intensity

$$S_0 = \frac{216 \nu k_B T}{\pi^2 \rho {d_p}^5 \left(\frac{\rho_p}{\rho}\right)^2 C_c} [m^2/s^3]. \tag{23}$$

Here, ξ_i is a Gaussian random number with zero mean and unit variance, k_B is the Boltzmann constant and T is the temperature. This formulation of Brownian diffusion is important for submicron particles.

4.2 Lagrangian modeling

To solve the Lagrangian-equation for a particular moving particle, the dynamic behavior of the gas phase (generally obtained by an Eulerian approach) and other particles surrounding this moving particle should be pre-determined. Since the particle velocity and the corresponding particle trajectory are calculated for each particle, this approach is more suitable to obtain the discrete nature of motion of particles. However, to obtain statistical averages with reasonable accuracy, a large number of particles will have to be tracked. An advantage of using the Lagrangian approach is the ability to easily vary the physical properties associated with individual particles such as diameter, density etc. More-over, local physical phenomena related to the particle flow behavior can be easily probed. Hence, the Lagrangian models can also be used for validation, testing, and development of continuum models [25].

The Lagrangian approach is classified into two types namely, Deterministic trajectory methods and Stochastic trajectory methods based on the effect of turbulence. In a deterministic method, all the turbulent transport processes of the particle phase are neglected whereas the stochastic method takes into account the effect of fluid turbulence on the particle motion by considering instantaneous fluid velocity in the formulation of the equation of particle motion.

$\vec{u}$ in Eq. 15 is the instantaneous fluid velocity. In a DNS approach, $\vec{u}$ is directly available as the instantaneous Navier-stokes equations are solved and the particles are tracked in the instantaneous velocity field. In a LES approach, the large energy containing scales are directly resolved by solving the filtered Navier-stokes equations. In all state-of-the-art commercial CFD solvers, the particles are tracked in the filtered velocity field and the effect of sub-grid-scales on the particle motion are neglected.

In a RANS approach, the time-averaged Navier-stokes equations are solved to obtain the time averaged mean flow velocity. The particles are tracked by constructing an instantaneous velocity filed by adding a velocity fluctuations to the mean velocity field. The velocity fluctuations are modeled through a stochastic approach. Stochastic modeling involves direct simulation of particle motion through a random turbulent flow field. There are several approaches in developing stochastic models. Few examples in literature includes the Discrete-Random-Walk (DRW) model, the Continuous-Random-Walk model (CRW), models based on random Fourier modes [32] and the pdf models [33]. In the present work, two modeling approaches are explored, namely the DRW model and the CRW model.

4.2.1 Discrete Random Walk model

One of the most frequently used model is the eddy interaction model (EIM) first introduced by Hutchinson et al. [34] and further developed by Gosman and Ioannides [35]. The EIM is also referred to as the Discrete-

Random-Walk (DRW) model.

$\vec{u}$ in Eq. 15 is the instantaneous fluid velocity represented as the sum of the mean and fluctuating velocity as follows:

$$u = \overline{u} + u^{'} \quad [m/s] \tag{24}$$

$$v = \overline{v} + v^{'} \quad [m/s] \tag{25}$$

$$w = \overline{w} + w^{'} \quad [m/s] \tag{26}$$

where $\overline{u}$, $\overline{v}$ and $\overline{w}$ are the time-averaged mean velocity components computed from a RANS simulation. $u^{'}$, $v^{'}$ and $w^{'}$ are the fluid fluctuating velocities defined as $\sqrt{\overline{u'^2}}$, $\sqrt{\overline{v'^2}}$ and $\sqrt{\overline{w'^2}}$. In most commercial CFD solvers, the fluid fluctuating velocity components are modeled assuming isotropic turbulence.

The chosen fluctuation is referred to a turbulent eddy whose size (length scale) and life-time(time scale) is known. Sommerfeld et al. [28] proposed the following relations for the eddy parameters:

$$t_e = 2\tau_L = c_t \frac{k}{\varepsilon} \tag{27}$$

and

$$l_e = t_e \sqrt{\frac{2}{3}k} \tag{28}$$

where, $c_t = 0.3$, t_e is the eddy time scale, l_e is the eddy length scale and τ_L is the Lagrangian time scale. It represents the time over which the velocity of a particle is self-correlated.

It is accepted that the fluctuation remains constant within a turbulent eddy for a certain interaction time, while the respective mean velocity component (U) is varied according to particle position. The interaction time is the minimum of two time scales, one being the turbulent eddy lifetime and the other is the crossing-time of the particle located within the eddy [35].

$$t_{int} = min(t_e, t_c) \quad [s] \tag{29}$$

The crossing-time is defined as

$$t_c = -\tau_p \, ln \left[1 - \left(\frac{l_e}{\tau_p |u - u_p|} \right) \right] \quad [s] \tag{30}$$

where τ_p is the particle relaxation time, l_e the eddy length scale and $|u - u_p|$ the magnitude of slip velocity.

In circumstances where $l_e/(\tau_p|u - u_p|) > 1$, Equation 30 has no solution. This can be interpreted as the particle trapped by an eddy, in which case $t_{int} = t_e$ [35]. This procedure may be repeated for as many interaction times as required for the particle to traverse the required distance. If a statistically significant number of particles are tracked in this way, the ensemble averaged behavior should represent the turbulent dispersion induced by the prevailing fluid field [35].

4.2.2 Continuous Random Walk model

Recently, [36, 37, 38, 39] presented in detail CRW model for the prediction of particle deposition in wall bounded flows. The main equations used in the modeling are presented here.

Within this approach, the particle deposition modeling is divided into two regions namely, the boundary layer region with strong anisotropic turbulence and bulk flow region with isotropic turbulence. The model is based on a Langevin equation. The Langevin equation takes different forms depending on the particle location which could be in the boundary layer or in the bulk region. In the **boundary layer region**, the normalized Langevin equation for streamwise, wall-normal and spanwise directions are given by:

$$d\left(\frac{u^{'}}{u_{rms}}\right) = -\left(\frac{u^{'}}{u_{rms}}\right).\frac{\Delta t}{\tau_L} + \sqrt{\frac{2}{\tau_L}}.d\xi_x \tag{31}$$

$$d\left(\frac{v^{'}}{v_{rms}}\right) = -\left(\frac{v^{'}}{v_{rms}}\right).\frac{\Delta t}{\tau_L} + \sqrt{\frac{2}{\tau_L}}.d\xi_y + \frac{\partial v_{rms}}{\partial y}.\frac{\Delta t}{1+Stk} \tag{32}$$

$$d\left(\frac{w^{'}}{w_{rms}}\right) = -\left(\frac{w^{'}}{w_{rms}}\right).\frac{\Delta t}{\tau_L} + \sqrt{\frac{2}{\tau_L}}.d\xi_z \tag{33}$$

where, $u^{'}$, $v^{'}$ and $w^{'}$ are the fluid fluctuating velocity components in streamwise, wall-normal and spanwise directions. u_{rms}, v_{rms} and w_{rms} are the corresponding RMS velocity components. x, y and z are the coordinates in x, y and z directions. ξ_x, ξ_y and ξ_z are the Gaussian random numbers with zero mean and variance dt.

In the above equation, Stk is a particle Stokes number, which is the ratio of particle relaxation time to the Lagrangian time scale and is given by:

$$Stk = \frac{\tau_p}{\tau_L}. \tag{34}$$

The last term in RHS of Eq. 32 is the mean drift correction term, which is added to avoid the un-physical migration of small inertial particles towards the boundary layer. [40] indicated that neglecting this term lead to overestimation of the particle deposition.

In the **bulk flow region**, the following equations for the normalized Langevin equations are solved for streamwise, wall-normal and spanwise directions:

$$d\left(\frac{u^{'}}{u_{rms}}\right) = -\left(\frac{u^{'}}{u_{rms}}\right).\frac{\Delta t}{\tau_L} + \sqrt{\frac{2}{\tau_L}}.d\xi_x + \frac{1}{3u_{rms}}.\frac{\partial k}{\partial x}.\frac{dt}{1+Stk} \tag{35}$$

$$d\left(\frac{v^{'}}{v_{rms}}\right) = -\left(\frac{v^{'}}{v_{rms}}\right).\frac{\Delta t}{\tau_L} + \sqrt{\frac{2}{\tau_L}}.d\xi_y + \frac{1}{3v_{rms}}.\frac{\partial k}{\partial y}.\frac{dt}{1+Stk} \tag{36}$$

$$d\left(\frac{w^{'}}{w_{rms}}\right) = -\left(\frac{w^{'}}{w_{rms}}\right).\frac{\Delta t}{\tau_L} + \sqrt{\frac{2}{\tau_L}}.d\xi_z + \frac{1}{3w_{rms}}.\frac{\partial k}{\partial z}.\frac{dt}{1+Stk} \quad (37)$$

where, k is the turbulent kinetic energy.

4.2.3 Eulerian statistics and time scales

In case of DRW, the Eulerian statistics of fluid fluctuating velocities $u^{'}$, $v^{'}$ and $w^{'}$ appearing in Eqs. 24, 25 and 26 needs to be specified. In most of the state-of-the-art commercial CFD solvers, the fluid fluctuating velocities are specified assuming isotropic turbulence. Most stochastic isotropic models in practical use are derived from Gosman and Ioannides [35] which is given by:

$$u^{'} = v^{'} = w^{'} = \sqrt{\frac{2}{3}k} * \zeta \quad [m/s] \quad (38)$$

where k is the turbulent kinetic energy which may be determined from any typical two-equation turbulence closure model such as the $k-\varepsilon$ model or the $k-\omega$ model. ζ is a random number drawn from a normal probability distribution with zero mean and unit standard deviation.

In the CRW approach, the fluid fluctuating velocities are defined from the Langevin equations. Depending on the region of interest, two sets of Langevin equations are solved. In the bulk flow region, Eqs. 35, 36 and 37 are solved to obtain the fluid fluctuating velocities $u^{'}$, $v^{'}$ and $w^{'}$. Assuming isotropic turbulence in the bulk fluid flow, the RMS velocities in Eqs. 35, 36 and 37 are given by:

$$u_{rms} = v_{rms} = w_{rms} = \sqrt{\frac{2}{3}k} \quad [m/s] \quad (39)$$

where, k is the turbulent kinetic energy.

In the near-wall region, Eqs. 31, 32 and 33 are solved to obtain the fluid fluctuating velocities $u^{'}$, $v^{'}$ and $w^{'}$. The RMS velocities in these equations needs to be prescribed based on anisotropic near-wall behavior of the RMS velocities. There are several correlations proposed in the literature to model the near-wall anisotropy. These correlations are discussed in detail in the next section.

To close the Langevin equations, the Lagrangian time scale τ_L must be specified. The Lagrangian time scale correlation approximated by the fits provided by [41] is used in the present work. In the boundary layer, the Lagrangian time scale is given as follows

$$\tau_L^+ \simeq 10 \qquad \text{for} \qquad y^+ < 5 \quad (40)$$

$$\tau_L^+ = 7.122 + 0.5731y^+ - 0.00129y^{+2} \qquad \text{for} \qquad 5 < y^+ < 200 \quad (41)$$

where, τ_L^+ is defined as

$$\tau_L^+ = \frac{\tau_L u^{*2}}{\nu} \tag{42}$$

Here, y^+ is the normalized wall distance, which is given by:

$$y^+ = \frac{yu^*}{\nu} \tag{43}$$

where, u^* is the friction velocity given by

$$u^* = \sqrt{\frac{\tau_w}{\rho}} \tag{44}$$

where, τ_w is the wall shear stress.

In the bulk flow, the Lagrangian time scale is given by:

$$\tau_L = \frac{2}{C_o}\frac{k}{\varepsilon} \tag{45}$$

where, C_o is constant with a value of 14 [42, 43].

4.2.4 Correlations for RMS velocities

In many applications, turbulence can be approximated as being isotropic in the bulk region when high swirls and rapid changes in the strain rate are not present. However, in the near-wall region, the turbulent velocity fluctuations are certainly strongly anisotropic. In fact, the RMS of the wall-normal component of velocity can be orders of magnitude smaller than the streamwise or the spanwise component (for example, see the DNS data of [10]). In order to consider this near wall anisotropic effect, there are several near-wall modifications proposed in the literature. The relevant modifications are summarized below.

Tian and Ahmadi

Based on the experimental measurements and the DNS data of [44, 45], it is well-known that continuity requires the wall-normal RMS turbulence velocity fluctuation to follow a quadratic variation [46]. Tian and Ahmadi [47] proposed the following correlation:

$$v_{rms} = Ay^{+2} \qquad \text{for} \qquad y^+ < 4 \tag{46}$$

where, $v_{rms} = \sqrt{v'^2}/u^*$. A value of A is suggested to be 0.008 using the DNS data of [45].

Kallio and Reeks

Based on several experimental data, [41] proposed to use the following near-wall correction to the wall-normal velocity fluctuation:

$$v_{rms} = \frac{0.005y^{+2}}{1 + 0.002923y^{+2.128}} \tag{47}$$

It was indicated that these correlations are valid in the near wall region where y^+ <200.

Matida et al.

Considering that the wall normal fluctuating component plays a major role in the particle deposition, [48] suggested to apply the wall-normal function proposed by [49] for all three fluctuating components as follows:

$$u_{rms} = v_{rms} = w_{rms} = [1 - exp(-0.02y^+)]\sqrt{\frac{2k}{3}} \tag{48}$$

The above formulation was applied for different y^+ ranges based on the flow-rate.

Wang and James

[49] introduced three functions f_u, f_v and f_w to specify the local RMS velocities close to the wall. These functions are derived from the DNS data of a channel flow [44, 50]. The RMS velocities were defined as:

$$u_{rms} = f_u\zeta\sqrt{\frac{2k}{3}} \tag{49}$$

$$v_{rms} = f_v\zeta\sqrt{\frac{2k}{3}} \tag{50}$$

$$w_{rms} = f_w\zeta\sqrt{\frac{2k}{3}} \tag{51}$$

ζ is a random number drawn from a Gaussian PDF with zero mean and unit variance. Functions f_u, f_v and f_w are given by:

$$f_u = 1 + 0.285(y^+ + 6)\exp[-0.455(y^+ + 6)^{0.53}] \tag{52}$$

$$f_v = 1 - \exp(-0.02y^+) \tag{53}$$

$$f_w = \sqrt{(3 - f_u^2 - f_v^2)} \tag{54}$$

It is pointed out that these functions are valid in the near-wall region where $y^+ <$80 and are Reynolds number dependent.

Dreeben and Pope

Based on the DNS fits of a channel flow (Re=13000), [51] proposed to use the following near-wall corrections velocity fluctuations in streamwise, wall-normal and spanwise directions as follows:

$$u^+_{rms} = \frac{\sqrt{\overline{u'^2}}}{u^*} = \frac{0.4y^+}{1 + 0.0239(y^+)^{1.496}} \tag{55}$$

$$v^+_{rms} = \frac{\sqrt{\overline{v'^2}}}{u^*} = \frac{0.116(y^+)^2}{1 + 0.0203(y^+) + 0.0014(y^+)^{2.421}} \tag{56}$$

$$w^+_{rms} = \frac{\sqrt{\overline{w'^2}}}{u^*} = \frac{0.19y^+}{1 + 0.0361(y^+)^{1.322}} \tag{57}$$

(58)

It was indicated that these correlations are valid in the near wall region where $y^+ <$100.

5 RANS modeling of particle transport and deposition

It is a known fact that accounting for near-wall anisotropy improves the particle deposition predictions. Regarding the near-wall anisotropy modeling, there are several uncertainties which need to be addressed such as: Which model is more accurate?; Is the DNS data near-wall Reynolds number dependent?; Is the DNS data near-wall geometry specific?; Different authors use different y^+ cut-off values below which anisotropy is considered. Which y^+ cut-off should be used?; In the viscous sub-layer (y^+¡5), different values of Lagrangian time scales are used. Which value of Lagrangian time scale yields best results?. The present chapter addresses all these uncertainties that exist in the RANS modeling of particle transport and deposition. By doing so, one would be able to come up with a robustly validated RANS model which can be used for nuclear applications.

5.1 DNS data for near-wall anisotropy

In the present section, it is discussed how near-wall DNS data from channel flows are used for near-wall anisotropic RANS modeling. Important questions addressed are: which near-wall model best fits the DNS data?; Is the DNS data Reynolds number dependent?; Is the DNS data geometry specific?.

5.1.1 Which near-wall correlation is accurate?

As seen in the previous chapter, there exist several correlations for the RMS velocities that can be used to account for the near-wall anisotropy. The not so trivial question is to understand which model is most accurate to be used for RANS modeling. The common factor among all the correlations is the fact that they are derived by fitting a correlation function to the existing experimental and/or DNS data in channel flows. In order to understand the differences, all the aforementioned correlations are plotted together and compared with the DNS data of Kim et al. [44].

Figure 5 shows the streamwise, wall-normal and spanwise RMS velocity distributions as a function of the non-dimensional wall distance. While the correlation of Matida et al. fits the wall-normal RMS velocity well, it severely underestimates the streamwise and the spanwise RMS velocity. The correlation of Kallio and Reeks for the wall-normal RMS velocity is far from the reference DNS data as this model was essentially derived in the 80's by curve-fitting to the then existing experimental data. All other correlations are consistent compared to the DNS data. The main outcome of this comparison is:

- Carefully choose a correlation which is accurately representing the DNS data. In the present compari-

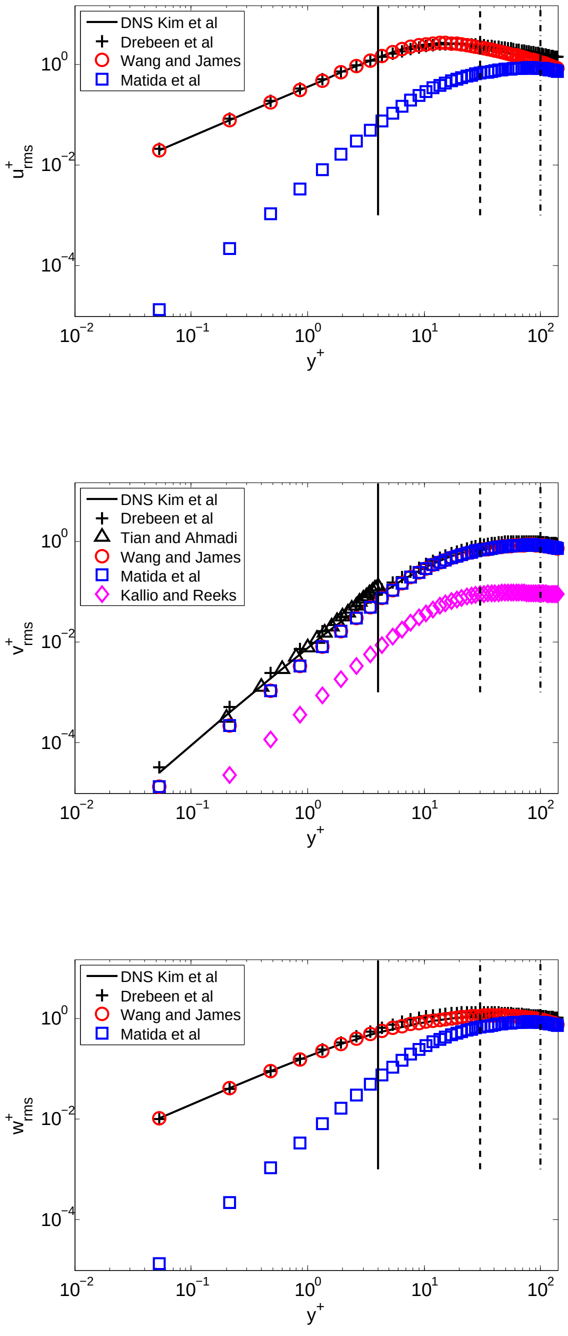

Figure 5   Comparison of various anisotropic near-wall correlations with the DNS data. Top: Streamwise RMS velocity; Middle: Wall-normal RMS velocity; Bottom: Spanwise RMS velocity.

son, both the Drebeen et al and the Wang and James correlations are showing best fit to the DNS data. Hence, either of these models can be used.

5.1.2 Is the near-wall DNS data Reynolds number dependent?

It is known that the RMS velocities are slightly dependent on the turbulent Reynolds number [52]. To investigate how sensitive the near-wall RMS velocities are to the change in Reynolds number, the existing DNS data in the literature are collected and plotted for a wide range of Re_τ. The DNS data are obtained from [44] and [53]. Fig. 6 shows the DNS data of RMS velocities for Re_τ ranging from 180 to 2000. It is observed that all three RMS velocity components are very much similar to each other up to $y^+ \sim 30$. Above y^+ 30, the DNS data starts to show visible Re_τ dependency. The main outcome of this comparison is:

- For y^+ <30, the DNS data shows no considerable sensitivity for a range of Re_τ. Hence, near-wall corrections can be applied up to y^+ of 30.

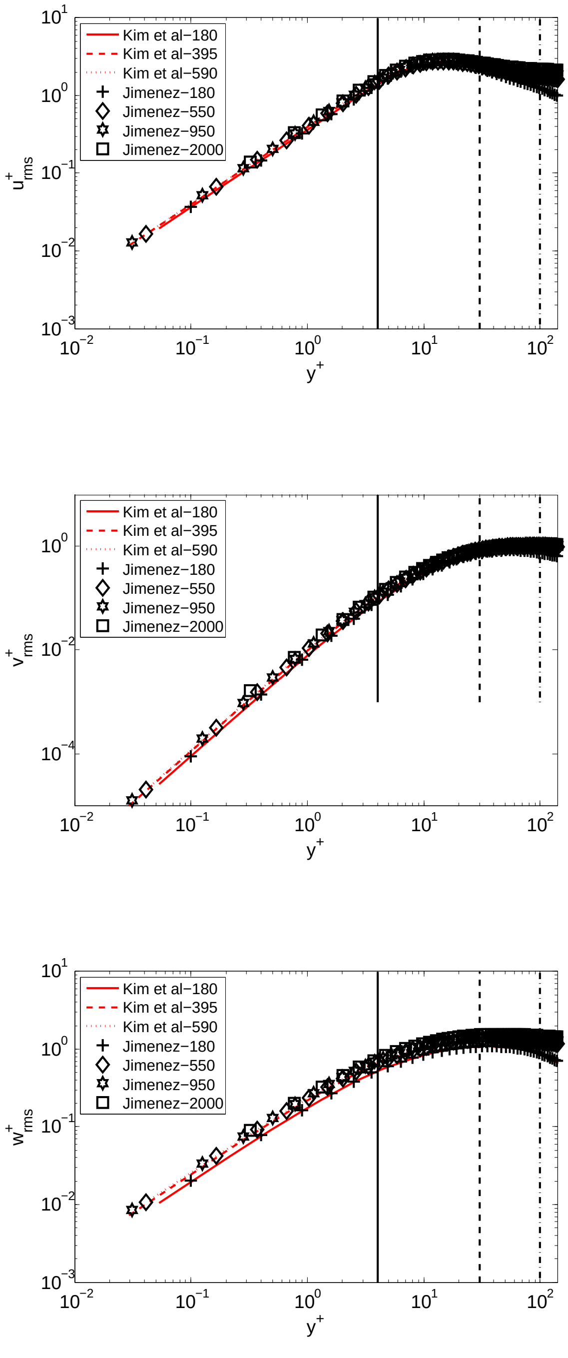

Figure 6   Comparison of DNS data for various Re_τ. Top: Streamwise RMS velocity; Middle: Wall-normal RMS velocity; Bottom: Spanwise RMS velocity.

5.1.3 Is the near-wall DNS data geometry specific?

Figure 7 shows the streamwise, wall-normal and spanwise RMS velocity distributions as a function of the non-dimensional wall-distance for two different flow configurations; a channel and a pipe. The streamwise and the spanwise RMS velocities show very similar profiles for the two different configurations. For the wall-normal RMS velocity, small deviations are observed below y^+ 30. The main outcome of this comparison is:

- The RMS velocity profiles are very similar for the channel flow and the pipe flow configurations at Re_τ 180 and 395.

So far, we have concluded that both the Drebeen et al. and the Wang and James correlations are showing best fit to the DNS data. For the present work, we chose to work with the Drebeen et al. correlation. It was also seen that the near-wall correlation can be applied upto y^+ 30 for a wide range of Reynolds numbers. Also, the near-wall correlation showed less sensitivity to the varying geometry configuration. Hence, it could be applied for different geometric configurations with fair degree of confidence.

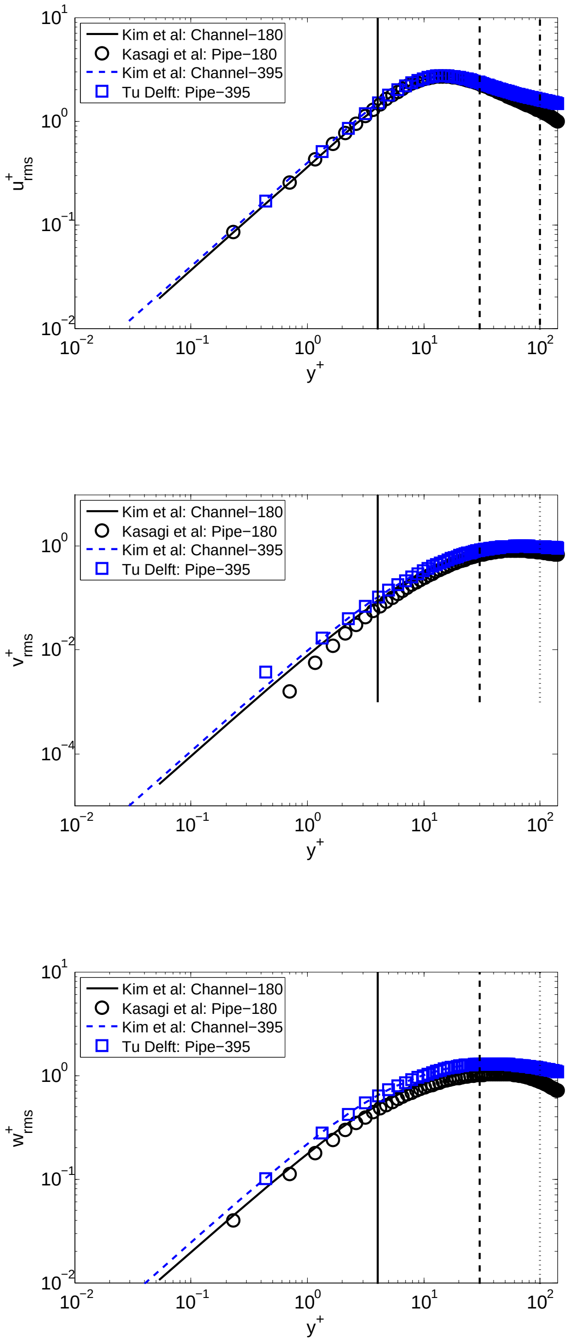

Figure 7 Comparison of DNS data for channel and pipe flows at Re_τ 180 and 395. Top: Streamwise RMS velocity; Middle: Wall-normal RMS velocity; Bottom: Spanwise RMS velocity.

5.2 Test Case

Now that a near-wall correlation to account for anisotropy is chosen in the previous section, there exist several uncertainties how to apply this near-wall correlation in a robust way. These uncertainties are addressed by performing sensitivity studies on a chosen test case. The test case chosen for the sensitivity analysis is described next.

The computational domain considered for the simulation corresponds to a 3D channel with a length, width and height of 0.4 m, 0.0628 m and 0.02 m, respectively. The computational domain is meshed using the ANSYS GAMBIT [54] meshing tool. A structural hexahedral grid is created with a cell dimension of 0.5 mm in all directions. A higher mesh resolution in the boundary layer is used with the first grid point at a distance of 0.05 mm away from the wall. A growth factor of 1.2 is used, which makes sure that cell sizes grow uniformly from the boundary layer to the bulk. It is worth mentioning that these cell dimensions are also used by [47]. The total number of cells in the mesh is about 6 million.

The initial air temperature and pressure is assumed to be 288 K and 1 bar. The air density and viscosity are taken to be 1.2 kg/m^3 and 1.84$\cdot$10^{-5} ns/m^2. The Reynolds number based on the channel width is 6667, which means the flow is turbulent. To model turbulence, a standard $k - \varepsilon$ turbulence model with enhanced wall treatment is used. Further details of the model can be found in [29]. A fully developed profile for the velocity, k and ε are applied at the inlet. The values of k and ε are assumed to be zero at the wall while, no-slip boundary condition for velocity is applied. At the outlet, a static atmospheric pressure is assumed. A periodic boundary condition in the spanwise direction is used for the 3D simulation.

The effect of different particle sizes on the deposition velocity are evaluated. For this purpose, different particle sizes ranging from 0.01 μm to 50 μm are considered. The particle density is assumed to be 2400 kg/m^3. The particles are injected at $x = 0.2m$ where a fully developed flow is observed. The particles are uniformly distributed at the bottom of the wall, between y^+ 0 and 30. The particles are injected with a velocity equal to the local air velocity. At the inlet and outlet, ”escape” boundary is applied. It implies that the particles leave the computational domain when it touches these boundaries. At the walls, ”trap” boundary condition is imposed. It implies that the particles stick to the wall as soon as they come in contact with the wall.

Since the simulation of a 3D channel is expensive for sensitivity studies, as a first step, a simulation is performed to assess whether the computational domain can be represented by a 2D channel. The results of the comparison in Fig. 8 shows that the 3D channel can be represented by a 2D channel with no considerable effects on the deposition velocity. Hence, for all further sensitivity simulations, a 2D channel is used as the

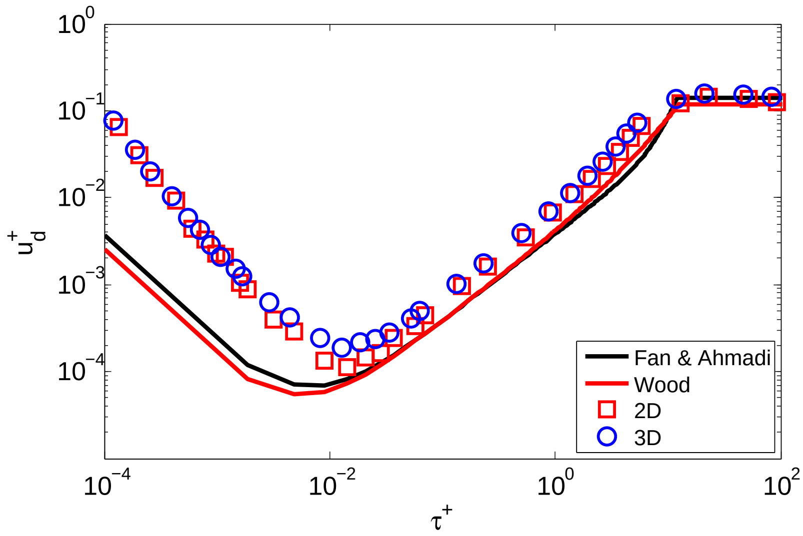

Figure 8 Comparison of deposition velocity between a 3D and a 2D channel.

computational domain.

5.2.1 Postprocessing method

The particle deposition is commonly characterized by non-dimensional deposition velocity:

$$u_d^+ = \frac{J}{C_0 u^*}[-] \tag{59}$$

The deposition velocity is given as a function of the normalized particle relaxation time τ^+. The above expression is valid for particles released with a uniform concentration C_0 near a surface. Here, J is the particle mass flux to the wall per unit time. The particle relaxation time is defined as:

$$\tau^+ = \frac{\tau u^{*2}}{\nu} = \frac{S{d_p}^2 u^{*2}}{18\nu^2} C_c[-] \tag{60}$$

where, S is the ratio of particle to fluid density. In our simulations, we obtained the particle deposition velocity [47] as follows:

$$u_d^+ = \frac{N_d/t_d^+}{N_0/y_0^+}[-] \tag{61}$$

where

$$y_0^+ = \frac{y_0 u^*}{\nu}[-] \tag{62}$$

and

$$t_d^+ = \frac{t_d u{*}^2}{\nu}[-] \tag{63}$$

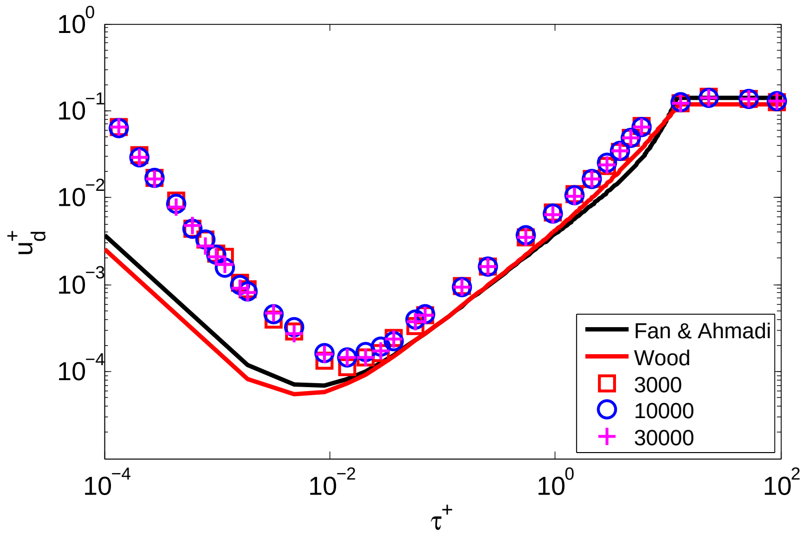

Figure 9 Comparison of deposition velocity between a 3D and a 2D channel.

Here, N_d is the number of deposited particles in the time duration of t_d^+ and N_0 is the initial number of particles uniformly distributed in a region within a distance of y_0^+ from the wall.

A value of 30 for y_0^+ is used, while N_0 is taken to be 3000. These values are also recommended by [47].

To investigate the influence of the initial number of particles N_0 on the deposition velocity statistics, additional simulations are performed with higher initial number of particles. The results in Fig. 9 shows that 3000 particles are sufficient to obtain particle number independent results.

5.2.2 Applied numerical schemes

The spatial discretization of the conservation equations are performed with a second-order upwind scheme. The pressure-velocity coupling is performed with the SIMPLE method and the discretized equations are solved using a segregated solver in an iterative manner.

There are several numerical schemes available within Fluent for the time integration of the particle motion, namely analytic, implicit, trapezoidal and the Runge-Kutta scheme. The performance of each of these schemes is assessed by simulating the horizontal channel with each of these schemes. The results in Fig. 10 show that there is no considerable difference between the four available methods. In the present work, the trapezoidal scheme is used for all the simulations.

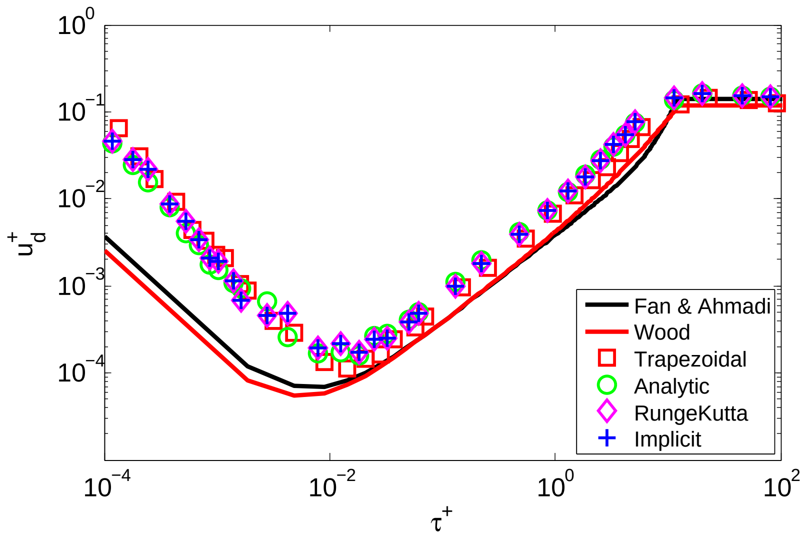

Figure 10 Performance of different time integration schemes for particle tracking in a 2D channel.

5.3 Fluid results

The mean streamwise velocity and the turbulent kinetic energy predictions by the standard $k - \varepsilon$ model are as shown in Fig. 11. While the mean streamwise velocity is predicted well in the near-wall region, the turbulent kinetic energy is underestimated. However, if one compares the turbulent kinetic energy to the three fluctuating components of velocity, it is apparent that the kinetic energy in the wall-normal and the spanwise directions are severely overestimated. As seen in the work of [47], this isotropic modeling of the turbulent kinetic energy in the near-wall leads to unreliable particle deposition predictions.

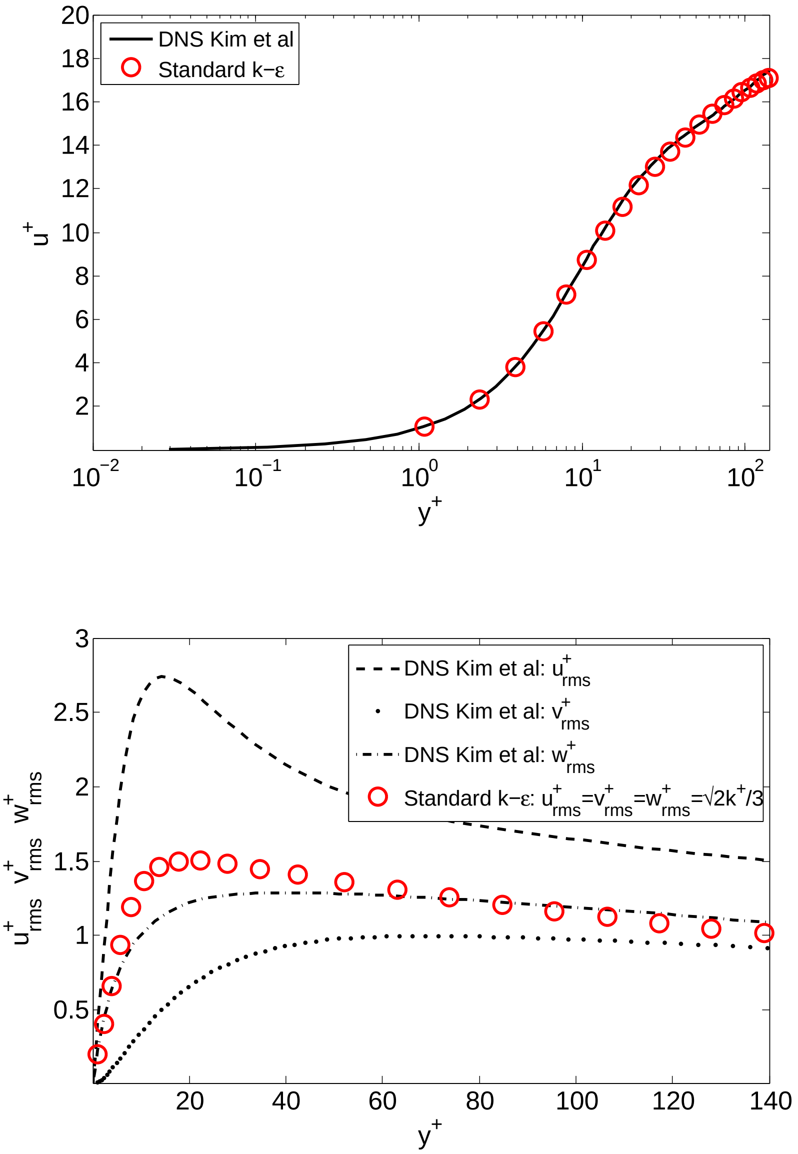

Figure 11 Comparison of flow predictions by the standard $k-\varepsilon$ model. (Above): Non-dimensional stream-wise mean velocity component; (Below): Non-dimensional turbulent kinetic energy.

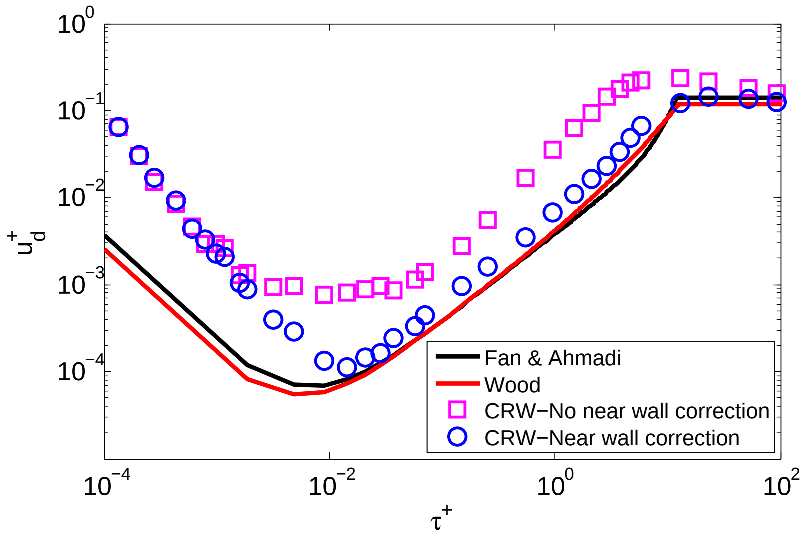

Figure 12 Comparison of the particle deposition velocity by the isotropic near-wall modeling vs. the anisotropic near-wall modeling.

5.4 Particle Results

5.4.1 Effect of near-wall correction

As seen before, there exist several correlations for the RMS velocities which can be used to account for the near-wall anisotropy. Based on careful evaluation, the correlation of Drebeen et al. is chosen for the present work. The importance of taking the near-wall anisotropy into account is addressed in here. Fig. 12 shows the comparison of the particle deposition velocity by the isotropic near-wall modeling vs. the anisotropic near-wall modeling. Clearly, accounting for the near-wall anisotropy has resulted in a better match of deposition velocities, especially for the non-dimensional relaxation times between 10^{-2} and 10. Below 10^{-2}, the results for both the isotropic and the anisotropic models are over-predicted. The particles in this range are predominantly deposited by the Brownian motion. Hence, the main reason for the over-prediction is the deficiency in the Brownian diffusion modeling.

The main outcome of this comparison is:

- Near-wall anisotropy is important and needs to be taken into account to obtain realistic deposition velocity predictions.

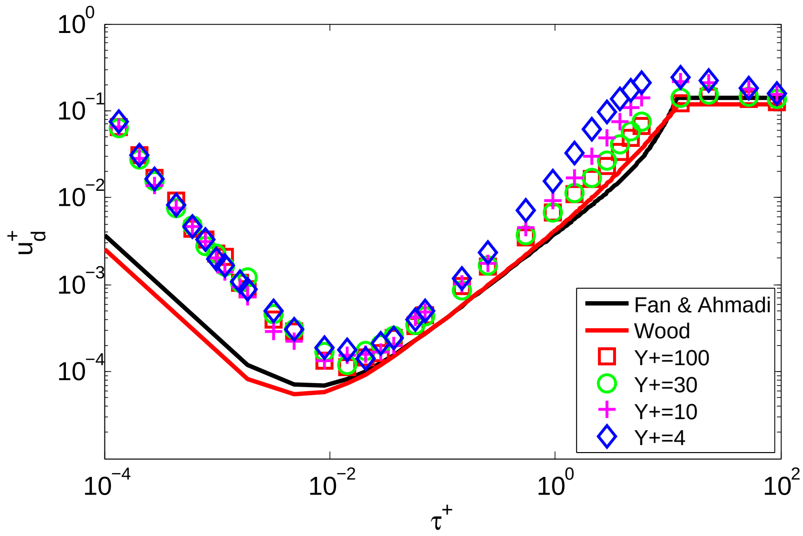

Figure 13 Particle deposition velocity predictions for different y^+ cut-off values.

5.4.2 Effect of y^+ cutoff

A lot of variability is seen in the literature with respect to the y^+ cut-off value below which the near-wall anisotropy is taken into account. For example, Tian and Ahmadi [47] propose to use their correlation below y^+ 4; Kallio and Reeks [41] propose to apply their correlation below y^+ 200; Wang and James [49] suggest to use their correlation below y^+ 80; Dreeben and Pope [51] suggest to use their correlation below y^+ 100. Considering that all these correlations are basically DNS fits, there is no clear reason for different y^+ cut-off values. Recognizing these differences, it becomes important to test the effect of the y^+ cut-off value on the deposition predictions. Fig. 13 shows the deposition velocity predictions for various y^+ cut-off values. Most of the sensitivity is observed for the particle relaxation times in the range 1 to 10. It is clear that a cut-off value of y^+ 30 and above is required to get a better deposition velocity prediction. Considering that the DNS data in the near-wall showed Reynolds number dependency after y^+ of 30, it is recommended to use y^+ of 30 as a cut-off.

The main outcome of this comparison is:

- A y^+ value of 30 is recommended as a cut-off value below which the near-wall anisotropy effects should be considered. Applying anisotropy below y^+ 30 leads to overestimation of the particle deposition velocity in a certain range of particle relaxation times.

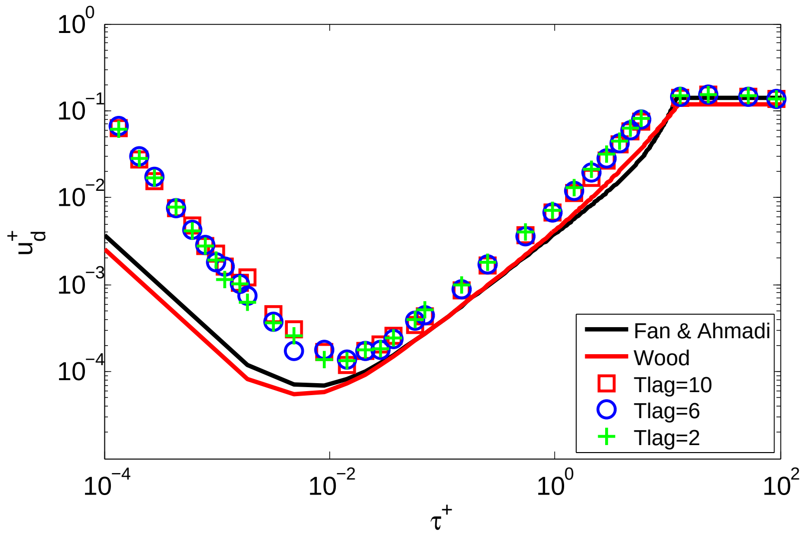

Figure 14 Particle deposition velocity predictions for different τ_L^+ cut-off values.

5.4.3 Effect of τ_L^+ value in the viscous sub-layer

The Lagrangian integral time scale τ_L^+ appearing in the Langevin equations is used to reproduce the turbulent dispersion of the particle phase. It represents the time over which the velocity of a particle is self correlated. τ_L^+ can generally be rigorously defined for homogeneous turbulence. For inhomogeneous turbulence, it is derived from either the Eulerian spectra of fluctuating velocities or from the Lagrangian calculations by evaluating the Lagrangian autocorrelations. In the present work, we use the fits provided by Kallio and Reeks [41]. For the viscous sub-layer ($y^+ < 5$), a constant value of 10 is recommended for τ_L^+. The Lagrangian DNS simulations of Bocksell and Loth [55] have estimated the wall normal component of the Lagrangian time scale to be between 2 and 6. The work of Luo et al. [56] have worked out an average value of the wall normal Lagrangian time scale to be between 3 and 5. Since a range of τ_L^+ are reported in the literature, the effect of it on the particle deposition velocity is tested here. Fig. 14 shows the deposition velocity predictions for τ_L^+ values of 2, 6 and 10. As seen, there is no considerable influence of this constant on the deposition velocity predictions.

The main outcome of this comparison is:

- The values of 2, 6 and 10 for τ_L^+ in the region below y^+ of 5 have no considerable effect on the deposition velocity predictions.

5.4.4 Effect of Reynolds number

It has been shown that the near-wall DNS statistics up to y^+ 30 are relatively universal for a wide range of Re_τ values ranging from 180 to 2000. The simulations so far were performed at a Reynolds number of 6667. In order to verify if one can apply the near-wall correlations at different Reynolds numbers, a channel flow simulation at 5 times higher Reynolds number is performed. Fig. 15 shows the deposition velocity predictions at two different Reynolds numbers. It is seen that the deposition velocity predictions at a higher Reynolds number are also consistent with the comparison data.

The main outcome of this comparison is:

- The present near-wall correlations can be applied to a wide range of Reynolds numbers.

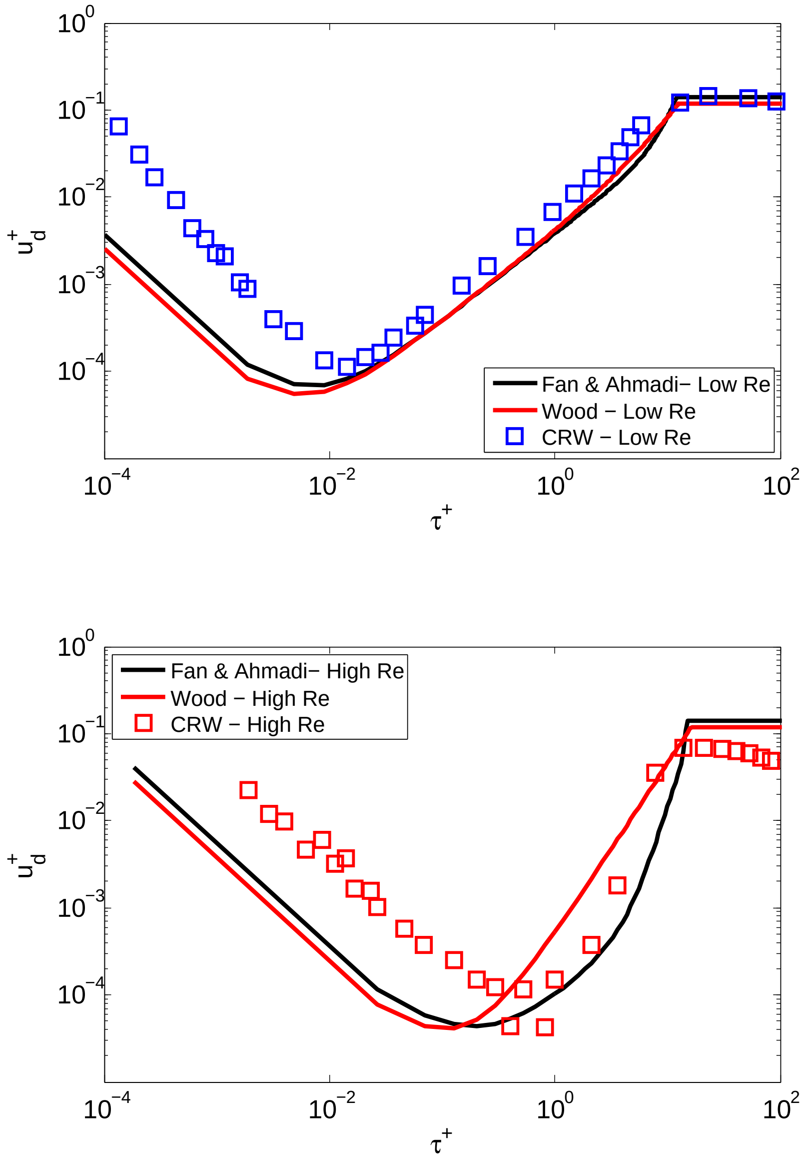

Figure 15 Particle deposition velocity predictions at different Reynolds numbers.

6 LES modeling of particle transport and deposition

The present chapter aims at presenting the generic validation simulations performed to assess the applicability of LES. Section 6.1 deals with results of deposition in a 90 ° bend pipe. Results of deposition in a square channel are given in Section 6.2.

6.1 Large Eddy Simulation of a 90° bend pipe

In this section, results of simulations of a bend pipe are discussed. In these simulations, particles with diameters ranging from 0.62 μm through 26.66 μm are released and the results on deposition given. First, the numerical setup is discussed, followed by the deposition results.

6.1.1 Geometry and mesh

The computational domain of the bend pipe is given in Fig. 16a. The diameter D of the pipe is 0.02m. The inlet is $1D$ long and the outlet is $2D$ long. The radius of the curvature of the bend is 0.056m, such that the curvature ratio R_0 is 5.6. In order to validate the numerical method, the mesh is made according to what is reported by Breuer [57]. The cross section contains 1.08×10^4 cells whereas Breuer uses 8.9×10^3 cells. Each cross section is composed of a part with hexahedral cells and a part with a pave mesh, see also Fig. 16b. The region near the wall is meshed with hexahedral cells. The nearest wall cell has its center at $y^+ = 0.35$ off the wall, similar to Breuer. The cells are stretched with a stretching ratio of 1.05 until the cell height equals $y^+ = 10$. The remaining inner part is meshed with a pave mesh in which a conformal mesh in radial direction is established. The mesh contains 195 evenly spaced cells in circumferential direction and 257 evenly spaced cells in streamwise direction.

6.1.2 Fluid dynamics model

The flow is simulated using Large Eddy Simulations (LES). Kolmogorovs theory of self similarity states that the large eddies of the flow are dependent on the geometry while the smaller scales are more universal. This is what LES is based on. Therefore, the large three-dimensional eddies which are dictated by the geometry and boundary conditions of the flow involved are directly resolved by the method whereas the small eddies which tend to be more isotropic are modeled via a subgrid-scale model. This has the advantage that the models are independent of the specific problem at hand. For the LES approach, the equations modeling the

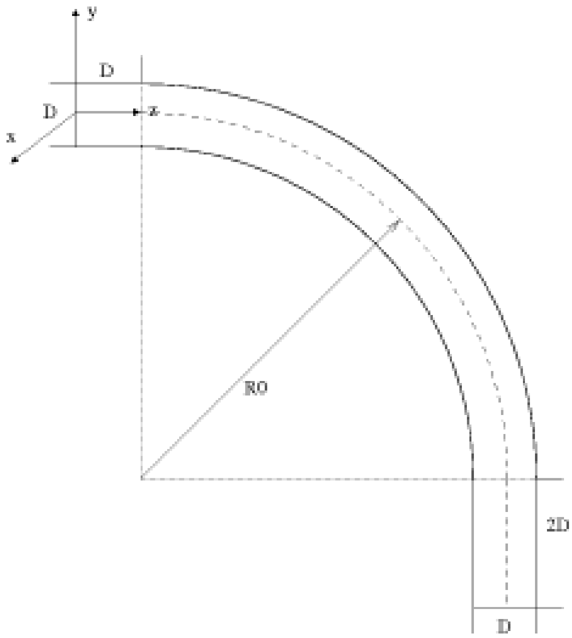

a Geometry of bend pipe

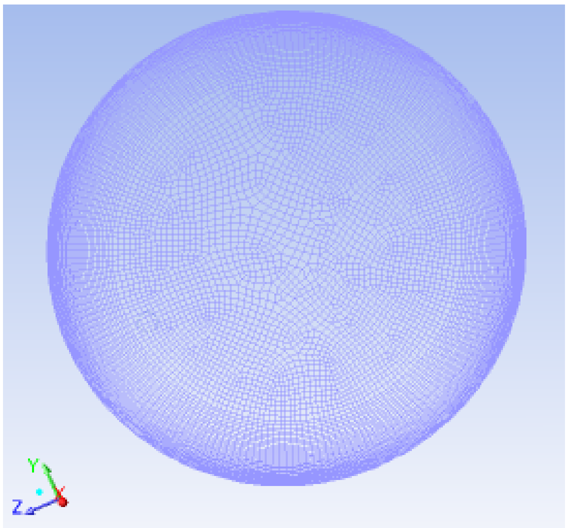

b Mesh of cross sections

Figure 16 Geometry and mesh of 90° bend pipe.

flow are filtered. The resulting filtered incompressible unsteady Navier-Stokes equations read:

$$\frac{\partial \bar{u}_j}{\partial x_j} = 0 \tag{64}$$

$$\frac{\partial \bar{u}_j}{\partial t} + \frac{\partial(\bar{u}_j\bar{u}_j)}{\partial x_j} = -\frac{\partial p}{\partial x_i} - \frac{1}{Re}\frac{\partial \tau_{ij}^{\mathrm{mol}}}{\partial x_j} - \frac{\partial \tau_{ij}^{\mathrm{SGS}}}{\partial x_j} \tag{65}$$

$$\tau_{ij}^{\mathrm{mol}} = -2\nu\bar{S}_{ij} \quad \text{where } \bar{S} = \frac{1}{2}\left(\frac{\partial \bar{u}_i}{\partial x_j} + \frac{\partial \bar{u}_j}{\partial x_i}\right) \tag{66}$$

where the overbar indicates the resolved scales. The Reynolds number is the characteristic flow Reynolds number.

The flow is assumed to be Newtonian. The physical properties of the fluid and particles are given in Table 4.

Density	1.3 kg/m^3
Viscosity	15.7×10^{-6} m^2/s
Density particles	895 kg/m^3
Reynolds number	10,000

Table 4 Physical properties of LES of bend pipe.

6.1.3 Boundary conditions

For the inflow conditions, the instantaneous flow field of a fully developed pipe flow is used. The outlet is modeled as a pressure outlet. At the wall, a no-slip boundary condition is used, because the grid resolution

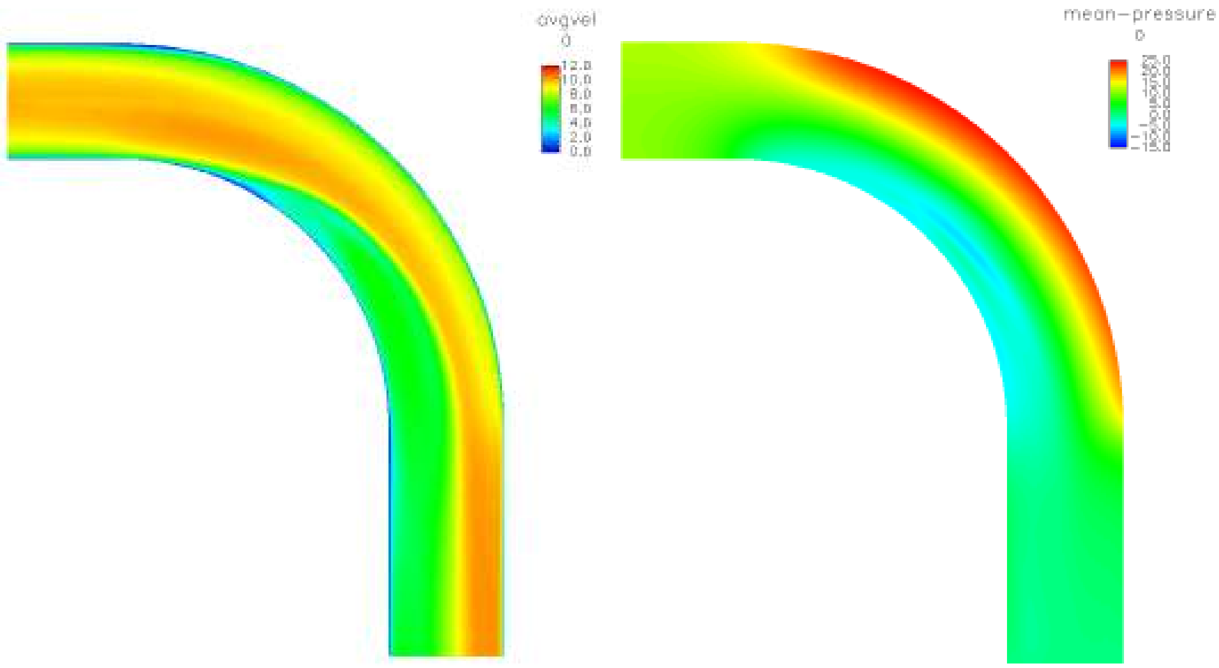

Figure 17   Time-averaged flow results of velocity (left) and static pressure (right).

near the wall is sufficient to resolve the viscous sublayer (Breuer [57]).

6.1.4 Main flow result

After 5 through flows ($t^+ = 3034$), the flow is found to be statistically stable. At this time, the particles are injected into the domain. Figure 17 shows the time-averaged velocity (left) and static pressure (right). The pressure is low at the inner radius of the bend and high at the outer radius. Fig. 18 shows the instantaneous flow field of the symmetry plane and the cross-section immediately after the bend. Turbulent structures can be seen here. Figure 19 shows the streamlines of the averaged turbulent flow at a cross-section at 90 degrees. The secondary flow structures are clearly visible here.

It is expected for a flow with a high Dean number ($De = Re/\sqrt{R_0} \approx 4225$) that secondary boundary layers develop on the wall with fluid entering these boundary layers near the outer bend and leaving near the inner bend [58].

6.1.5 Particulate phase

The particles are spherical with a range in diameter of $0.62 - 26.66\mu m$. The particles have a density ρ_p such that $\rho_p/\rho_f \gg 1$. This allows us, according to Breuer [57], to take only drag, gravity and buoyancy into account. Furthermore, the concentration of particles is low enough to apply one-way coupling. The particles are injected at the inlet of the pipe. They are uniformly distributed with a distance of 1 mm. The particles are injected during 100 time steps (0.09TF, $t^+ = 61$) and tracked for 2.5 TF ($t^+ = 1668$). After

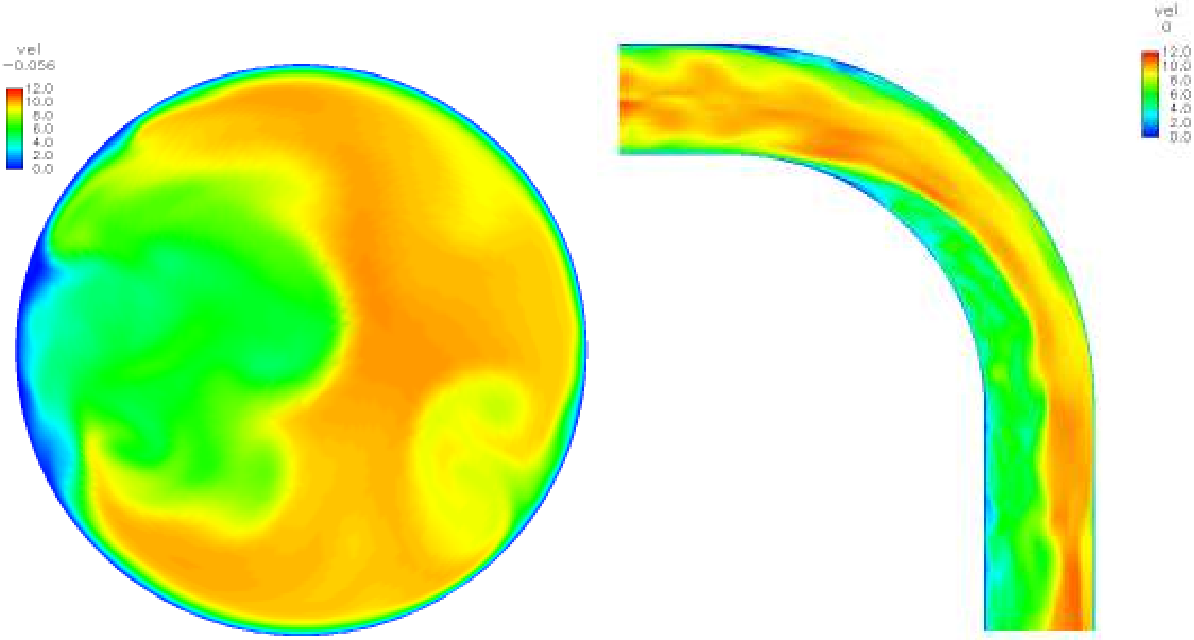

Figure 18   Instantaneous flow field of the midplane (left) and the cross-section immediately after the bend.

this amount of time more than 99% of the particles have either deposited on the wall or left the flow domain at the outlet.

The deposition efficiency is obtained via:

$$\eta = \frac{N_{dep}}{N_{out} + N_{dep}} \tag{67}$$

where N_{dep} is the number of deposited particles and N_{out} is the number of particles that have left the pipe at the exit, which is also used by Berrouk [58].

6.1.6 Deposition result

The result for $St = 0.005...1.53$ is given in Figure 20 in which the fraction of deposited particles (η) is plotted against the Stokes number. From the figure it follows that for small Stokes numbers, the comparison with both experimental and numerical data is very good. For mediate Stokes numbers the deposition efficiency is largely overpredicted and for the large Stokes numbers the deposition efficiency is slightly overpredicted.

Fig. 21 shows the fraction of deposited particles along the running coordinate s of the bend with respect to the total number of particles in the flow with the same Stokes number. The line s is the dashed line in the figure of the geometry Fig. 16a and is the centerline of the pipe. The figure shows that there is a higher fraction of deposited particles with large inertia. This is in agreement with the result shown in Fig. 20. It is also clear that the particles deposit mainly in the bend of the pipe. In the inlet ($0 < x < 0.02$) very few

Figure 19 Streamlines of time-averaged flow immediately after the bend.

particles deposit. It is interesting to note that the used method predicts no deposition just before the bend for the smaller Stokes numbers. This is contrary to the result of Breuer, in which a small number of particles deposited in the whole inlet.

In Fig. 21 the fraction of deposited particles along the perimeter of the bend with respect to the total number of particles in the flow with the same Stokes number is plotted. The outer bend is at 90°. The figure shows that at majority of the particles deposit at the outer bend. At the inner bend, particles tend to deposit too, according to the used numerical method. It is, however interesting to see that Breuer [57] has a dent in the curves at the position of the inner bend. We explain our result by noting that at the inner bend the two counter rotating vortices are present which influence the deposition of the particles.

In Figure 22 the deposition of three different particle sizes on the bend is shown. In the left figure it is clear that the smaller particles do follow the main stream pattern after the bend. For the medium sized particles, 14.7 μm, the deposition is larger in the bend compared to the 4.77 μm particles and after the bend the particles seem to follow the secondary flow structures. For the largest particles, 25.30 μm, most deposit on the wall. A few will exit the pipe and they do that by following the main stream pattern.

6.2 Deposition in a channel

The deposition of particles with a small diameter (3 - 30 μm) in a channel has been simulated using LES applying two different turbulent Reynolds numbers. In this section the set-up and the results of the simulations are given. The result of the deposition is compared with the experimental result of Barth [59].

6.2.1 Geometry and mesh

The geometry of the channel resembles that of the channel in which experiments were conducted. For the computational domain, the channel consists of a square inlet of 0.1 x 0.1 m. The channel is 1 m long, equal to the test section of the experimental channel, see Barth [59].

The grid is uniform in streamwise direction. In spanwise and normal direction the cells are stretched from $y^+ = 0.7$ to $y^+ = 10$. This results in about 0.5 million cells ($Re_\tau = 267$).

6.2.2 Fluid dynamics model

The same LES model as for the bend pipe case is used here. Additionally, a RANS simulation is performed to compare to the results of the LES simulation for the case with $Re_\tau = 267$. For the RANS simulation, a unsteady SST $k - \epsilon$ model is used. The time step is $1 \times 10^{-4} s$.

The turbulent Reynolds number is based on the friction velocity of $u_\tau = 0.08 m/s$ ($Re_\tau = 267$) and $u_\tau = 0.21 m/s$ ($Re_\tau = 700$). The flow is assumed to be Newtonian. The physical properties of the fluid and particles are given in Table 5.

6.2.3 Boundary conditions

The inlet and outlet have a periodic boundary condition. This makes it possible to apply a fully developed velocity profile at the inlet when the flow in the channel is developed, which happens at approximately 5 trough flows. The top, bottom and side walls are modeled with a no-slip boundary condition in order to simulate the experimental conditions.

6.2.4 Particulate phase

The spherical, rigid particles are injected according to the method in Lecrivain [60]. At the inlet of the channel 40,000 particles for each diameter are released in a virtual square area of $y^+ = 30$ at the centerline on the bottom. The particles are tracked for one trough flow of the bulk flow.

The deposition velocity is obtained via:

$$V_{dep} = \frac{N_{dep} t_{avg}}{N_0 / h} \, [-] \tag{68}$$

where N_{dep} is the number of deposited particles, t_{avg} the average time a particle needs to deposit, N_0 the total number of injected particles and h the maximum height at which the particles are released, which equals to $y^+ = 30$. This equation is an estimation of the ratio of the surface particle mass flux and the aerosol particle concentration [60].

Particles with a diameter ranging from $3.2\mu m$ to $33\mu m$ are injected. This covers the range of the diameters that were used in the experiment [59].

6.2.5 Flow result

Figures 23 shows the streamwise velocity component of the LES simulation at $Re_\tau = 267$.

6.2.6 Deposition result

In Fig. 24 the deposition velocity at $Re_\tau = 267$ is plotted against the dimensionless particle response time τ_p^+. It is given by:

$$\tau_p^+ = \frac{\rho_p {d_p}^2}{18\mu_g} \frac{u_\tau^2}{\nu} \, [-] \tag{69}$$

where τ_p^+ has been made dimensionless by multiplication with $\frac{u_\tau^2}{\nu}$.

From the figure it follows that the result of the LES simulation is significantly closer to the experiment than the result of the RANS simulation. Also, the numerical results differ in trend on log-log scale: a linear one for the LES results and an exponential one for the RANS results.

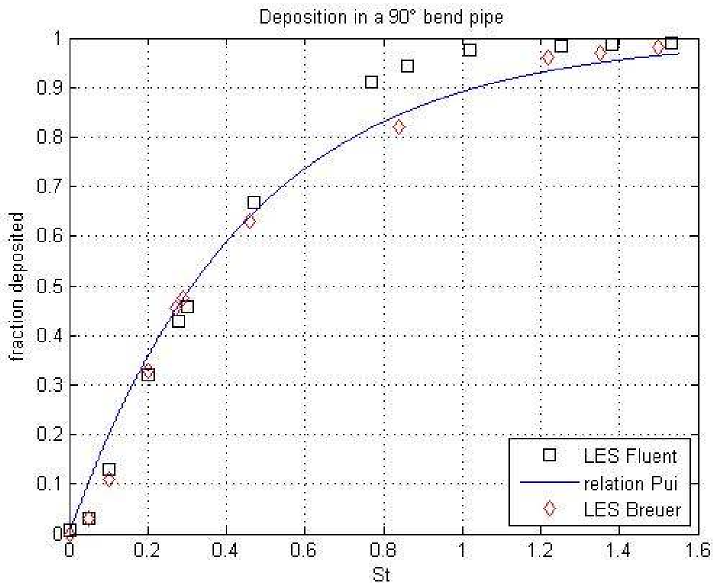

Figure 20 Deposition efficiency vs Stokes number for a 90° bend pipe with $Re = 10,000$.

Density	1.3 kg/m^3
Viscosity	$15.7 \times 10^{-6}\ m^2/s$
Density particles	895 kg/m^3
Turbulent Reynolds number	267, 700

Table 5 Physical properties of LES of square channel.

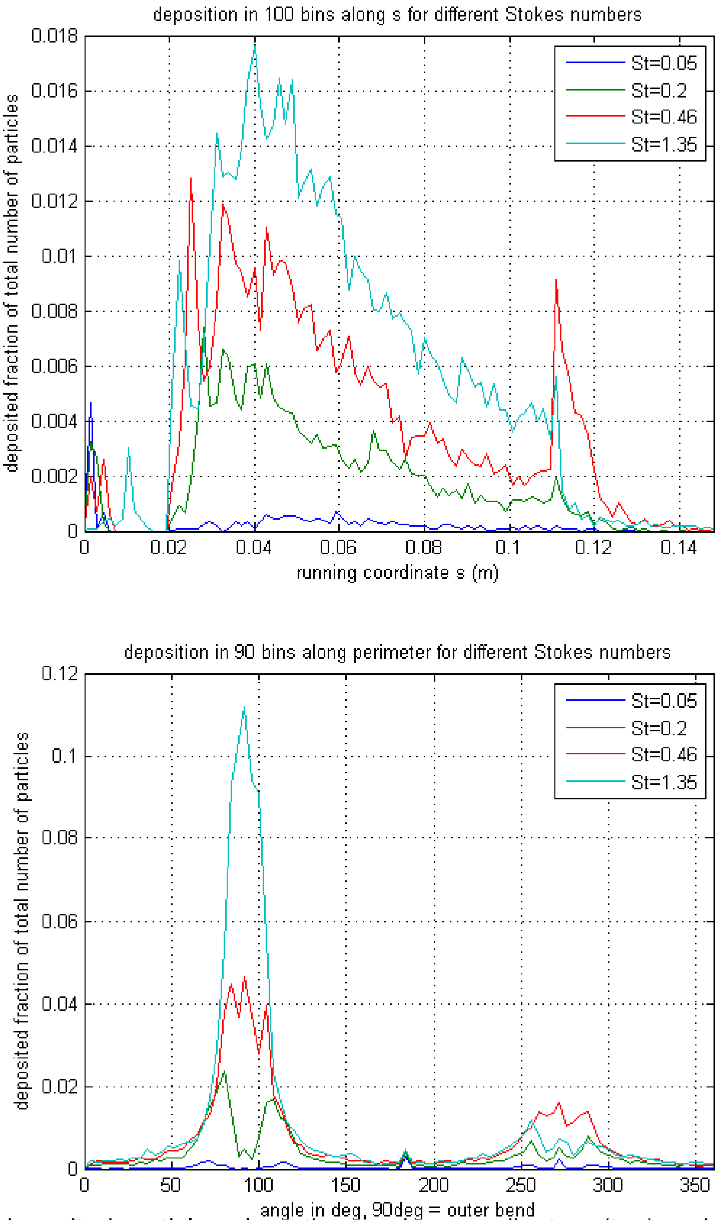

Figure 21 Fraction deposited particles along the running coordinate s (top) and the perimeter ϕ (bottom) for a 90° bend pipe with $Re = 10,000$.

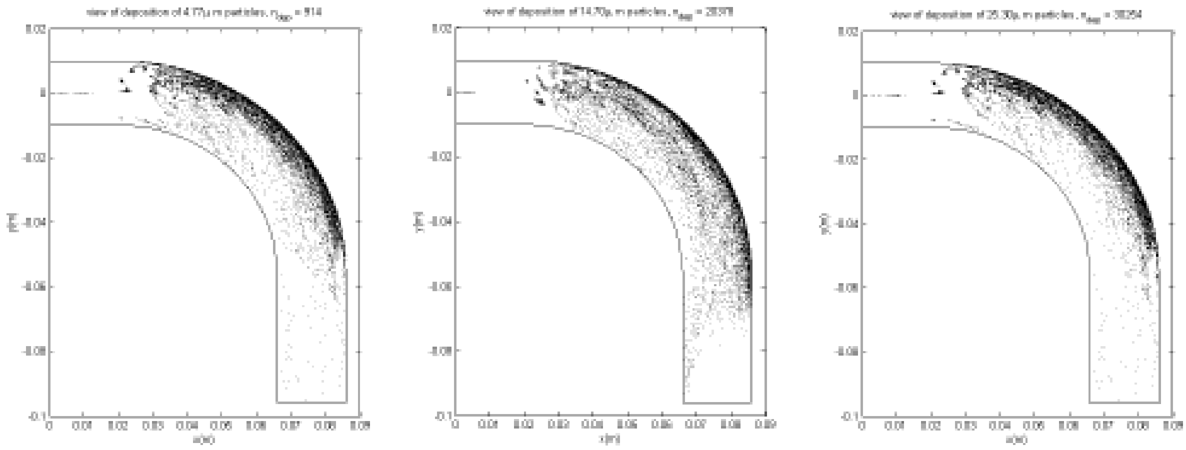

Figure 22 Side view of deposition in the bend for three different particles sizes.

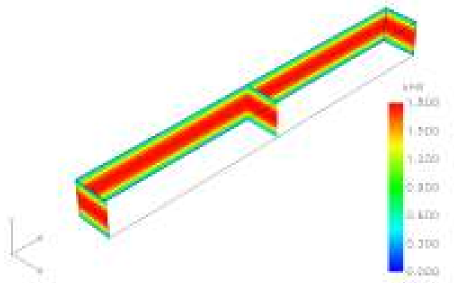

u-component

Figure 23 Velocity components in streamwise direction and three cross-sections.

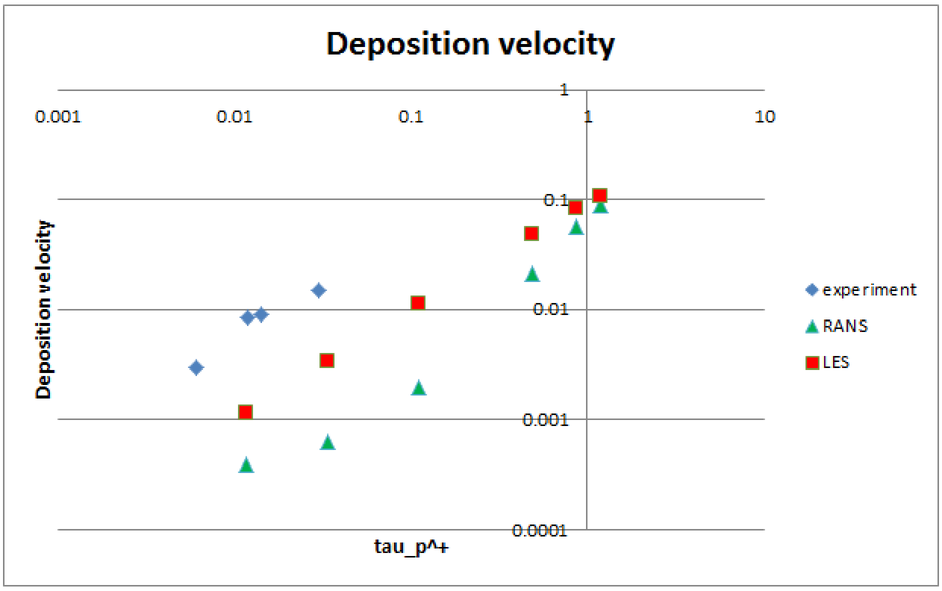

Figure 24 Deposition results of a square channel with $u_\tau = 0.08$.

7 Conclusions

The main conclusions from this work are as follows:

- Several correlations exist in the literature to model the near-wall anisotropy in the particle phase. Carefully choose a correlation which is accurately representing the DNS data. In the present work, both the Drebeen et al. and the Wang and James correlations are showing good fits to the DNS data. Hence, either of these models can be used.
- For y^+ <30, the DNS data showed no considerable sensitivity for a range of Re_τ. Hence, near-wall corrections can be applied up to y^+ of 30.
- The RMS velocity profiles are very similar for the duct flow and the pipe flow configurations at Re_τ 180 and 395 implying negligible sensitivity to changing geometry.
- From the fluid flow results, it is apparent that the kinetic energy in the wall-normal and the spanwise directions is severely over-estimated. Hence, there is the need for anisotropic correlations close to the wall.
- There were no considerable differences in the particle deposition patterns predicted by the CRW model and the DRW model.
- Particle deposition predictions show that the near-wall anisotropy is important and needs to be taken care of in order to obtain realistic deposition velocity predictions.
- A y^+ value of 30 is recommended as a cut-off below which the near-wall anisotropy effects should be considered. Applying anisotropy below y^+ 30 leads to over-estimation of particle deposition velocity in a certain range of particle relaxation times.
- The values of 2, 6 and 10 for τ_L^+ in the region below y^+ of 5 have no considerable effect on the deposition velocity predictions.
- The present near-wall correlations can be applied to a wide range of Reynolds numbers.
- LES shows improvements in results, especially for small Stokes number particles where RANS needs anisotropic modeling.
- Even though LES is more accurate, the applicability is limited to low Re.
- It is a good tool to use in the regions where the flow is in transitional regime, like the coolers.

References

[1] M P Kissane, F Zhang, and M W Reeks. Dust in htrs: Its nature and improving prediction of its resuspension. *Nuclear Engineering and Design*, doi:10.1016/j.nucengdes.2011.10.028, 2011.

[2] M P Kissane. A review of radionuclide behaviour in the primary system of a vhtr. *Nuclear Engineering and Design*, 239:3076–3091, 2009.

[3] H Gottaut and H Kruger. Results of experiments at the avr reactor. *Nuclear Engineering and Design*, 121:143–153, 1990.

[4] X W Luo, S Y Yu, Z S Zhang, and S Y He. Estimation of graphite dust quantity and size distribution of graphite particle in htr-10. 26(2):203–208, 2005.

[5] E Komen. Literature review in RAPHAEL. 21346/04.60264/C Rev. 2, 2009.

[6] R Baumer. Avr-experimental high-temperature reactor. 21 years of successfull operation for a future energy technology. *Association of German Engineers (VDI) - The society for energy technologies*, VDI verlag, Dusseldorf, 1990.

[7] D C Wilcox. *Turbulence modeling for CFD*. DCW Industries, Inc, California, 1998.

[8] H Schlichting. *Boundary layer theory*. McGraw-Hill, New York, 1979.

[9] J Young and A Leeming. A theory of particle deposition in turbulent pipe flow. *Journal of Fluid Mechanics*, 340:129–159, 1997.

[10] C Marchioli, A Soldati, J G M Kuerten, B Arcen, A Taniere, G Goldensoph, K D Squires, M F Cargnelutti, and L M Portela. Statistics of particle disperion in DNS of wall-bounded turbulence: Results of an international collaborative benchmark test. *International Journal of Multiphase Flow*, 34:879–893, 2008.

[11] H Zhang and G Ahmadi. Aerosol transport and deposition in vertical and horizontal turbulent duct flows. *Journal of Fluid Mechanics*, 406:55–80, 2000.

[12] C Narayanan, D Lakehal, L Botto, and A Soldati. Mechanisms of particle deposition in a fully developed turbulent open channel flow. *Physics of Fluids*, 15-3:763–775, 2003.

[13] C Marchioli, A Giusti, M V Salvetti, and A Soldati. Direct numerical simulation of particle wall transfer and deposition in upward turbulent pipe flow. *International Journal of Multiphase Flow*, 29:1017–1038, 2003.

[14] C F You, G H Li, H Y Qi, and X C Xu. Motion of micro-particles in channel flow. *Atmospheric Environment*, 38:1559–1565, 2004.

[15] A W Vreman. Turbulence characteristics of particle-laden pipe flow. *Journal of Fluid Mechanics*, 584:235–279, 2007.

[16] C Marchioli, M V Salvetti, and A Soldati. Some issues concerning large eddy simulation of intertial particle dispersion in turbulent bounded flows. *Physics of Fluids*, 20, 2008.

[17] R Zamansky, I Vinkovic, and M Gorokhovski. Acceleration of inertial particles in wall bounded flows DNS and LES with stochastic modelling of the subgrid acceleration. *13th European Turbulence Conference*, 318, 2011.

[18] B Y H Liu and J K Agarwal. Experimental observation of aerosol deposition in turbulent flow. *Journal of Aerosol Science*, 5-2:145–158, 1974.

[19] D D McCoy and T J Hanratty. Rate of deposition of droplets in annular two-phase flow. *International Journal of Multiphase Flow*, 3:319–331, 1977.

[20] D Y H Pui, F R Novas, and B Y H Liu. Experimental study of particle deposition in bends of circular cross section. *Aerosol Science and Technology*, 7-3:301–315, 1987.

[21] A R McFarland, H Gong, A Muyshondt, W B Wente, and N K Anand. Aerosol deposition in bends with turbulent flow. *Environ. Sci. Technol.*, 31:3371–3377, 1997.

[22] T M Peters and D Leith. Particle deposition in industrial duct bends. *Ann. occup. Hyg.*, 48-5:483–490, 2004.

[23] M R Sippola and W W Nazaroff. Particle deposition in ventilation ducts: Connectors, bends and developing turbulent flow. *Aerosol Science and Technology*, 39:139–150, 2005.

[24] H Jiang, L Lu, and K Sun. Experimental study and numerical investigation of particle penetration and deposition in 90 degree bent ventilation ducts. *Building and Environment*, 46:2195–2202, 2011.

[25] J S Curtis and B V Wachem. Modeling particle-laden flows: A research outlook. *Wiley InterScience*, 50-11, 2004.

[26] S E Elghobashi. On predicting particle-laden turbulent flows. 52:309–329, 1994.

[27] C Crowe, M Sommerfeld, and Y Tsuji. *Multiphase flows with droplets and particles*. CRC press, Boca Raton, 1998.

[28] M Sommerfeld, A Ando, and D Wennerberg. Swirling, particle-laden flows through a pipe expansion. *ASME: Journal of Fluids Engineering*, 114:648–656, 1992.

[29] FLUENT. Fluent user's guide 6.3, 2006.

[30] P G Saffman. The lift on small sphere in a slow shear flow. *Journal of Fluid Mechanics*, 22:385–398, 1965.

[31] P G Saffman. Corrigendum to: The lift on small sphere in a slow shear flow. *Journal of Fluid Mechanics*, 31:624–, 1968.

[32] M R Maxey. The gravitational settling of aerosol particles in homogeneous turbulence and random flow fields. *Journal of Fluid Mechanics*, 174:441–465, 1987.

[33] J Pozorski and J P Minier. The pdf method for lagrangian two-phase flow simulations. *Gas Particle Flows*, 1995.

[34] P Hutchinson, G F Hewitt, and A E Dukler. Deposition of liquid or solid dispersions from turbulent gas streams: a stochastic model. *Chemical Engineering Science*, 26:419–439, 1971.

[35] A D Gosman and E Ioannides. Aspects of computer simulation of liquid-fuelled combustor. *AIAA Journal*, 81-0323, 1981.

[36] A Dehbi. A CFD model for particle dispersion in turbulent boundary layer flows. *Nuclear Engineering and Design*, 238:707–715, 2008.

[37] A. Dehbi. Turbulent particle dispersion in arbitrary wall-bounded geometries: A coupled CFD-Langevin-equation based approach. *International Journal of Multiphase Flow*, 34(9):819 – 828, 2008.

[38] A. Dehbi. A stochastic Langevin model of turbulent particle dispersion in the presence of thermophoresis. *International Journal of Multiphase Flow*, 35(3):219 – 226, 2009.

[39] A. Dehbi. Validation against dns statistics of the normalized langevin model for particle transport in turbulent channel flows. *Powder Technology*, 200(1-2):60–68, 2010.

[40] Gregory. Influence of the Lagrangian integral time scale estimation in the near wall region on particle deposition. *Journal of Fluids Engineering*, 134(7), 2012.

[41] G A Kallio and M W Reeks. A numerical simulation of particle deposition in turbulent boundary layers. *International Journal of Multiphase Flow*, 15-3:433–446, 1989.

[42] Y. Mito and T.J. Hanratty. A stochastic description of wall sources in a turbulent field. part 2. calculation for a simplified model of horizontal annular flows. *Int. Jorunal of Multiphase Flow*, 30:803–825, 2004.

[43] Y. Mito and T.J. Hanratty. Use of a modified Langevin equation to describe turbulent dispersion of fuid particles in a channel flow. *Flow Turbulence and Combustion*, 68:1–26, 2002.

[44] J Kim, P Moin, and R D Moser. Turbulent statistics in fully developed channel flow at low reynolds number. *Journal of Fluid Mechanics*, 177:133–166, 1987.

[45] H. Ounis, G. Ahmadi, and J.B. McLaughlin. Brownian particle deposition in a directly simulated turbulent channel flow. *Physics of Fluids A*, 5:1427–1432., 1993.

[46] J.O.Hinze. *Turbulence*. New York: Mcgraw Hill, 1975.

[47] L Tian and G Ahmadi. Particle deposition in turbulent duct flows - comparison of different model predictions. *Journal of Aerosol Science*, 38:377–397, 2007.

[48] E A Matida, W H Finlay, C F Lange, and B Grgic. Improved numerical simulation of aerosol deposition in an idealized mouth-throat. *Journal of Aerosol Science*, 35:1–19, 2004.

[49] Y Wang and P W James. On the effect of anisotropy on the turbulent dispersion and deposition of small particles. *International Journal of Multiphase Flow*, 25:551–558, 1999.

[50] N.N. Mansour, J. Kim, and P. Moin. Reynolds-stress and dissipation-rate budgets in a turbulent channel flow. *Journal of Fluid Mech*, 194:15–44, 1988.

[51] T. D. Dreeben and S. B. Pope. Probability density function and Reynolds-stress modeling of near-wall turbulent flows. *Physics of Fluids*, 9(1):154–163, 1997.

[52] J. M. J. den Toonder and F. T. M. Nieuwstadt. Reynolds number effects in a turbulent pipe flow for low to moderate re. *Physics of Fluids*, 9(11), 1997.

[53] J. Jimenez and S. Hoyas. Turbulent fluctuatations above the buffer layer of wall-bounded flows. *J. Fluid Mech. Vol. 611, pages 215-236.*, 611:215–236, 2008.

[54] GAMBIT. Gambit user's guide 2, 2001.

[55] T.L. Bocksell and E. Loth. Stochastic modeling of particle diffusion in a turbulent boundary layer. *International Journal of Multiphase Flow*, 32:1234 – 1253, 2006.

[56] H Y Luo, Y Liu, and X L Yang. Particle deposition in obstructed airways. *Journal of Biomechanics*, 40:3096–3104, 2007.

[57] M Breuer, H T Baytekin, and E A Matida. Prediction of aerosol deposition in 90 degree bends using LES and an efficient lagrangian tracking method. *Journal of Aerosol Science*, 37:1407–1428, 2006.

[58] Abdallah Sofiane Berrouk. *Stochastic Lagrangian Modelling for Large Eddy Simulation of Dispersed Turbulent Two-Phase Flows*. Bentham Books, 2011.

[59] T. Barth. Experimental report and electronic data repository for the gas/graphite experiments. Technical Report WP:4.1.3, THINS, 2013.

[60] Grégory Lecrivain and Uwe Hampel. Influence of the Lagrangian Integral Time Scale Estimation in the Near Wall Region on Particle Deposition. *Journal of Fluids Engineering*, 134:074502–1, 2012.